

AD-A260 965

ION PAGE

Form Approved
OMB No. 0704-0188

2



Make 1 hour per response, including the time for reviewing instructions, searching existing data sources, the collection of information. Send comments regarding this burden estimate or any other aspect of this Washington Headquarters Services, Directorate for Information Operations and Reports, 1215 Jefferson Management and Budget, Paperwork Reduction Project (0704-0188), Washington, DC 20503

1. AGENCY USE ONLY (Leave blank)		2. REPORT DATE 1/29/1993	3. REPORT TYPE AND DATES COVERED Interim technical 1 July 1992 to 31 December 1992	
4. TITLE AND SUBTITLE Scanning tunneling microscopy of III-V semiconductors			5. FUNDING NUMBERS DAAL03-91-G-0054	
6. AUTHOR(S) John D. Dow			7. PERFORMING ORGANIZATION REPORT NUMBER	
7. PERFORMING ORGANIZATION NAME(S) AND ADDRESS(ES) Department of Physics Arizona State University Tempe, AZ 85287-1504			8. PERFORMING ORGANIZATION REPORT NUMBER	
9. SPONSORING / MONITORING AGENCY NAME(S) AND ADDRESS(ES) U. S. Army Research Office P. O. Box 12211 Research Triangle Park, NC 27709-2211			10. SPONSORING / MONITORING AGENCY REPORT NUMBER ARO 28508.3-EL	
11. SUPPLEMENTARY NOTES The view, opinions and/or findings contained in this report are those of the author(s) and should not be construed as an official Department of the Army position, policy, or decision, unless so designated by other documentation.				
12a. DISTRIBUTION / AVAILABILITY STATEMENT Approved for public release; distribution unlimited.			12b. DISTRIBUTION CODE	
13. ABSTRACT (Maximum 200 words) We report the first scanning tunneling microscopy images with atomic resolution of steps on the (110) surfaces of InAs, InP, and InSb, and we propose models of the surface geometries which lead to those steps. Relaxation of the step edges is interpreted in terms of dimerization of neighboring atoms. These studies of steps provide the basic foundation for future work oriented toward understanding the roles of steps as nucleation centers during growth of nanostructures and the importance of step defects in ultra-small devices.				
14. SUBJECT TERMS InAs, InP, InSb, Scanning tunneling microscopy			15. NUMBER OF PAGES 10	
			16. PRICE CODE	
17. SECURITY CLASSIFICATION OF REPORT UNCLASSIFIED	18. SECURITY CLASSIFICATION OF THIS PAGE UNCLASSIFIED	19. SECURITY CLASSIFICATION OF ABSTRACT UNCLASSIFIED	20. LIMITATION OF ABSTRACT UL	

DTIC
 ELECTE
 FEB 22 1993
 S E D

93-03263
 71P8

28508-EL

PROGRESS REPORT
TWENTY COPIES REQUIRED

1. ARO PROPOSAL NUMBER: 28508-EL
2. PERIOD COVERED BY REPORT: 1 JULY 1992 - 31 DECEMBER 1992
3. TITLE OF PROPOSAL: Scanning Tunneling Microscopy of III-V Semiconductors
4. CONTRACT OR GRANT NUMBER: DAAL03-91-G-0054
5. NAME OF INSTITUTION: Arizona State University
6. AUTHOR OF REPORT: John D. Dow
7. LIST OF MANUSCRIPTS SUBMITTED OR PUBLISHED UNDER ARO SPONSORSHIP DURING THIS REPORTING PERIOD, INCLUDING JOURNAL REFERENCES:

Accession For	
NTIS CRA&I	<input checked="" type="checkbox"/>
DTIC TAB	<input checked="" type="checkbox"/>
Unannounced	<input type="checkbox"/>
Justification
By	
Distribution /	
Availability Codes	
Dist	Avail and/or Special
A-1	

DTIC QUALITY INSPECTED 3

Y. Liang, W. E. Packard, and J. D. Dow. Fabrication of quantum dots on the InSb (110) surface. Superlatt. Microstruct. 11, 461-463 (1992). (MS 266)

M.-H. Tsai, W.-M. Hu, J. D. Dow, and O. F. Sankey. Relaxation of the ZnTe and CuCl (110) surfaces. J. Vac. Sci. Technol. A 10, 2511-2514 (1992). (MS 275)

M.-H. Tsai, C. S. Chang, J. D. Dow, and I. S. T. Tsong. Electronic contributions to scanning-tunneling-microscopy images of an annealed β -SiC(111) surface. Phys. Rev. B 45, 1327-1331 (1992). (MS 277)

H. Feil, H. J. W. Zandvliet, M.-H. Tsai, John D. Dow, and I. S. T. Tsong. Random and ordered defects on ion-bombarded Si(100)-(2x1) surfaces. Phys. Rev. Letters 69, 3076-3079 (1992). (MS 281)

Y. Liang, M.-H. Tsai, W. E. Packard, and J. D. Dow. Ethereal "interstitials" on the (110) surface of InSb. Solid State Commun. in press. (MS 288)

Y. Liang, W. E. Packard, and J. D. Dow. Steps on the (110) surface of InP. Proc. Mater. Res. Soc. in press. (MS 292)

Y. Wei, M.-H. Tsai, J. D. Dow, and I. S. T. Tsong. A dislocation-like antiphase boundary on a Si(111)-(7x7) surface. Submitted. (MS 294)

8. SCIENTIFIC PERSONNEL SUPPORTED BY THIS PROJECT AND DEGREES AWARDED DURING THIS REPORTING PERIOD:

William E. Packard, John D. Dow.

9. REPORT OF INVENTIONS (BY TITLE ONLY): None.

John D. Dow
Department of Physics and Astronomy
Arizona State University
Tempe, Arizona 85287-1504

BRIEF OUTLINE OF RESEARCH FINDINGS

1) As integrated circuits are miniaturized, the surface becomes a large fraction of each device, and its influence on device performance becomes greater. Moreover, a detailed understanding of semiconductor surfaces is needed for the fabrication of heterostructures and superlattice-based devices. Because very little is known about the surfaces of III-V compound semiconductors, we have launched a major program to understand their surfaces and native defects on those surfaces. This report focusses on InAs, InP, and InSb, and the defects we have observed on their (110) surfaces. To our knowledge, these are the first observations of such step-structure defects on these surfaces.

We have been among the first to obtain real-space atomic-resolution scanning tunneling microscopy images of the (110) surfaces of InAs, InP, and InSb cleaved in ultra-high vacuum (UHV). We observed steps of several- and one-atom height on these surfaces, as well as images of single atoms. Fig. 1 shows individual In atoms on a flat InAs (110) surface, imaged under positive bias (which reveals only the In atoms). Each bump is an In atom spaced from its neighbors by several Ångströms. In addition to flat terraces, we also observed steps in three principal directions: along (110), (111), and (112) directions. An example on the UHV-cleaved InP(110) surface, showing all three types of steps is given in Fig. 2, where the three types of steps meet to form a raised triangular terrace.

It is widely believed (but not directly demonstrated) that atomic-layer-by-layer growth by molecular beam epitaxy (and other methods) is initiated at such steps on (001) surfaces. Therefore we have tried to understand the structure and dynamics of these steps. We observed periodic variations in geometric structure along some of these steps, suggesting that the step-edges reconstruct. Therefore we have proposed models of the nature of the steps and their reconstructions in these cases. Fig. 3 shows an example of the observed periodicity along a (112)-type step on InAs(110). Our atomic model of this step is presented in Fig. 4 and Fig. 5. The experimental data indicate a periodicity of $6.7 \pm 0.8 \text{ \AA}$. In the model, which proposes a one-atom-high step, dimers form at the step edge, between the top and the bottom terrace. The theoretical periodicity is 7.4 \AA , in agreement with the data. We have also proposed a similar model of the (111)-type step edge and its reconstruction. Thus we have laid the foundation for studying steps and their roles in growth and surface reactions.

2) We are continuing our studies of STM imaging with a semiconductor tip,

reported previously.

3) We are studying the effects of electrical current (and its direction) on step edges and the domain populations of externally strained Si(100) 2x1. These are atomic-level electromigration studies. These experiments are being done in collaboration with Dr. Ig Tsong. He is providing the graduate student and we are providing the equipment.

4) In October of 1992 Dr. Ruth Nicolaides of Picatinny Arsenal, in Dover, New Jersey visited as part of an on-gong collaboration.

5) Our ARO research has benefitted from interaction with Pachyderm Scientific Industries, a spun-off company that deals in STM hardware and software.

Copies of abstracts of each paper are attached.

There has been continuing communication, including visits by William Packard to Dr. Ruth Nicolaides of Picatinny Arsenal, and by Dr. Ruth Nicolaides from Picatinny to our program.

Our File: report.arol93.rno

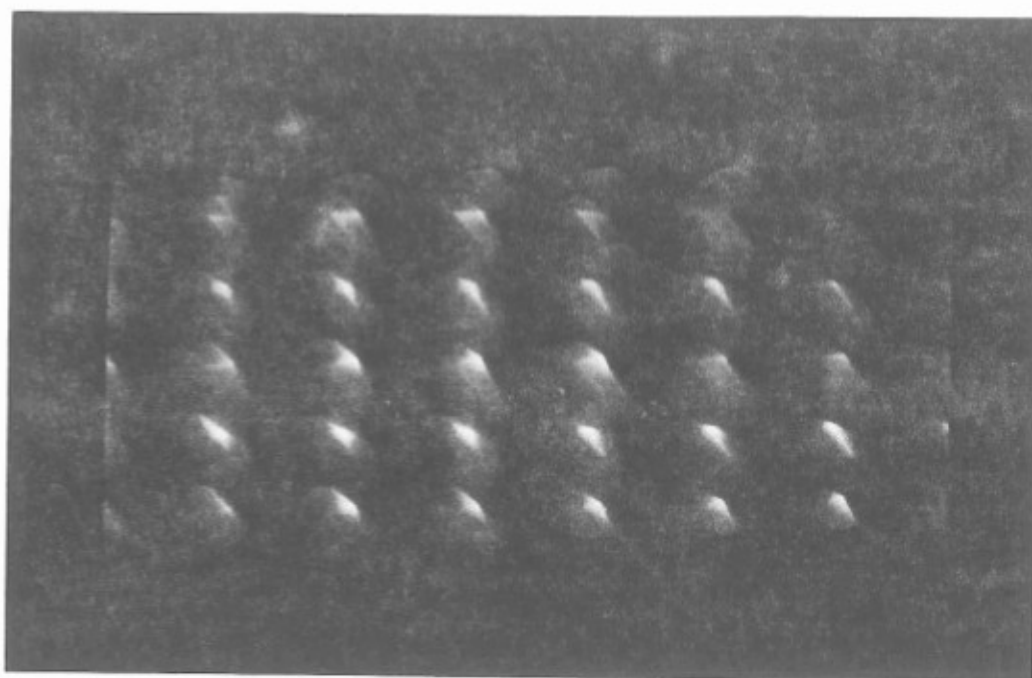


Fig. 1. Scanning tunneling microscopy image of the flat InAs(110) surface cleaved in ultra-high vacuum. The sample bias is +0.5 V, and so only the In atoms are visible. The tunneling current is 100 pA, and the image size is 40 Å x 18 Å.



Fig. 2. Triangular terrace observed by scanning tunneling microscopy of the InP(110) surface. This terrace is formed by intersection of (110), (111), and (112) steps. The image is 450 Å x 450 Å, taken at a bias of +2.0 V and a current of 100 pA.



Fig. 3. Scanning tunneling microscope image of a one-atom-high (110)-type step on the InAs(110) surface. The observed periodicity along the step edge is $6.7 \pm 0.8 \text{ \AA}$, and is attributed to dimerization.

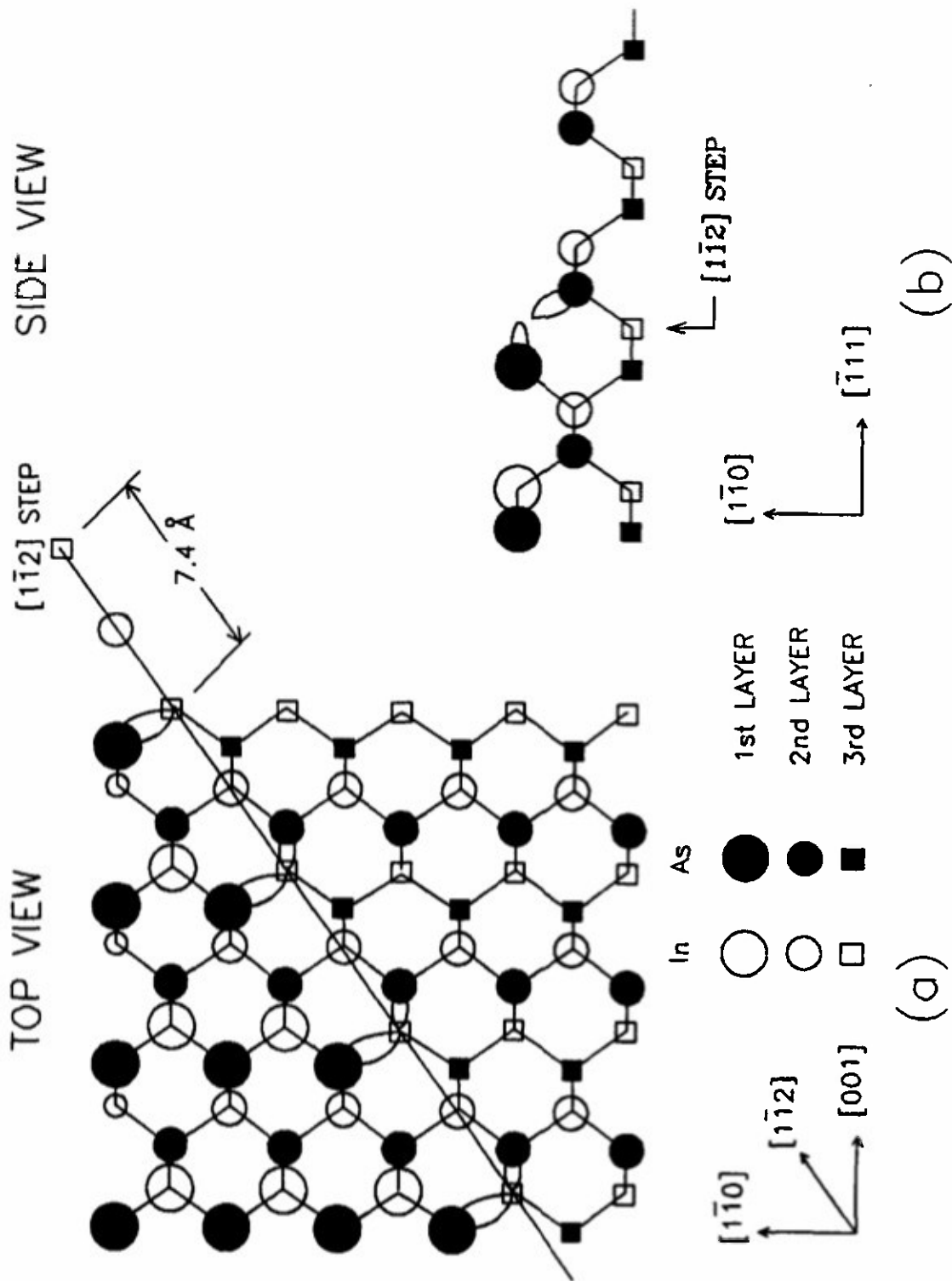


Fig. 4. Dimerization model for a $[112]$ -type step edge on $\text{InAs}(110)$, a $[1\bar{1}2]$ step, before any reconstruction or relaxation. (a) Top view of the step. (b) Side view, showing dangling bonds as "rabbit ears" prior to dimerization.

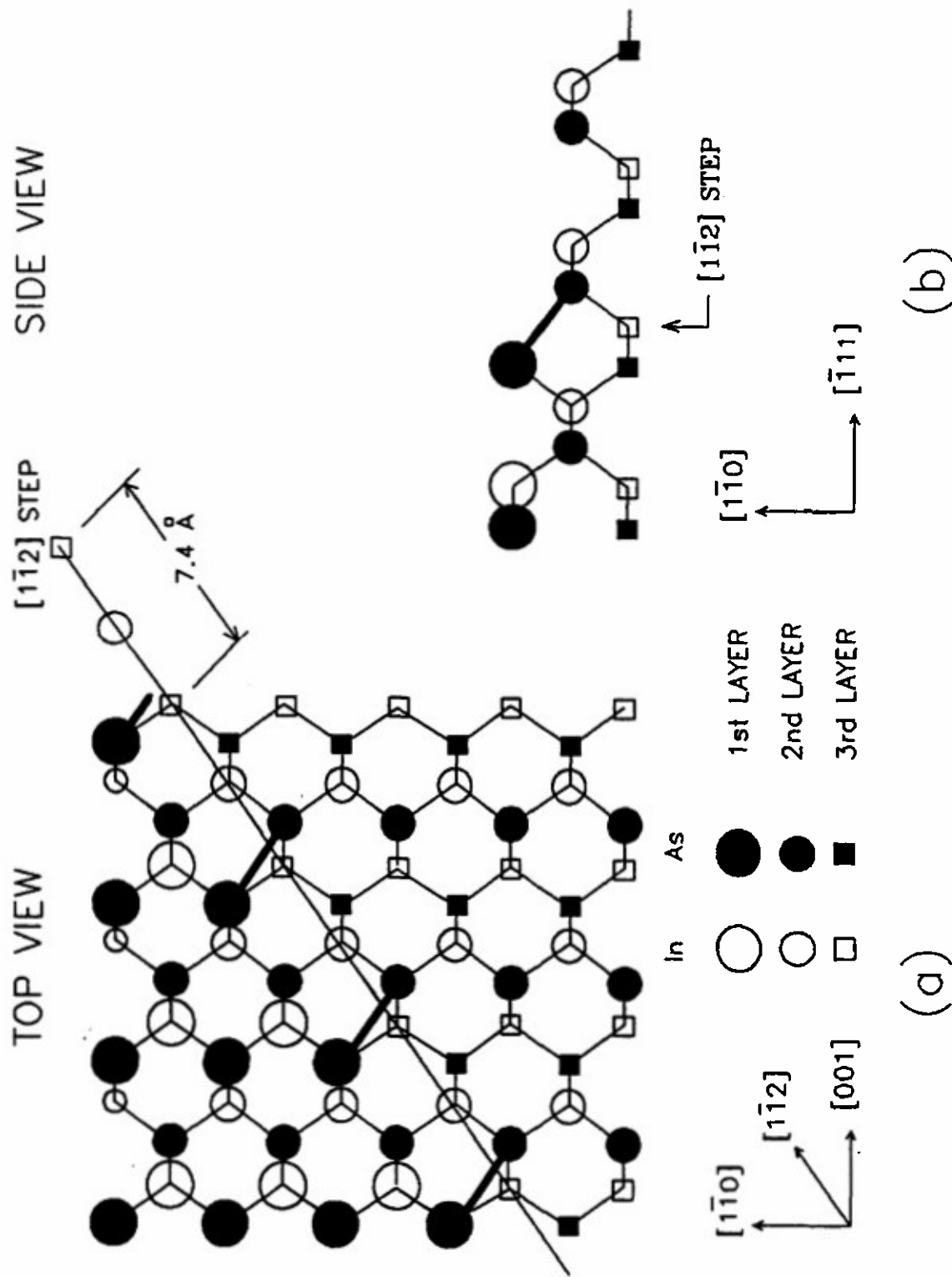


Fig. 5. Dimerization model for a (112) -type step edge on $\text{InAs}(110)$, a $[1\bar{1}2]$ step, after reconstruction and relaxation. (a) Top view of the step. (b) Side view, showing dangling bonds after dimerization. For simplicity of presentation, the usual 29° rigid rotation of the anions up out of the surface plane has been omitted.

Electronic contributions to scanning-tunneling-microscopy images of an annealed β -SiC(111) surface

M.-H. Tsai, C. S. Chang, John D. Dow, and I. S. T. Tsong

Department of Physics, Arizona State University, Tempe, Arizona 85287-1504

(Received 15 July 1991)

The reconstruction of the cubic β -SiC(111) surface was studied after annealing at -1200°C . The surface consistently showed a $6\sqrt{3}\times 6\sqrt{3}$ geometry when measured by low-energy electron diffraction (LEED) and a 6×6 geometry when imaged by scanning tunneling microscopy (STM). To resolve the discrepancy, we carried out first-principles calculations of the electronic structure of a surface model in which a graphite monolayer was incommensurately grown on top of the Si-terminated β -SiC(111) surface. The calculated energy band and density-of-states diagrams provide an explanation to the observed differences in LEED and STM results. They also explain the voltage-dependent contrast-reversal phenomenon observed in the STM images of the annealed surface.

I. INTRODUCTION

Scanning-tunneling-microscopy (STM) images are known to sample the local density of electronic states near the Fermi level at a surface. In certain cases, these images can be associated with the atomic geometry of the surface, the most well known of which is the Si(111)- 7×7 ,¹ provided that the surface electronic structure is closely tied to individual surface atoms. In other cases, image interpretations are not so straightforward, e.g., in Si(111)- $(\sqrt{3}\times\sqrt{3})\text{Al}$,² O on GaAs (110),³ and Si(111)- $(\sqrt{3}\times\sqrt{3})\text{Ag}$.^{4,5} Nevertheless, in the majority of cases, STM images do reflect the surface geometry and periodicity shown in LEED patterns. In the course of our studies on the reconstructions of the cubic β -SiC(111) surface,^{6,7} however, we found a disagreement between the surface geometry determined by STM and that determined by LEED. STM images show a 6×6 geometry while the LEED pattern indicates a $6\sqrt{3}\times 6\sqrt{3}$ geometry. To explain this discrepancy, we have invoked a model originally proposed by van Bommel, Crombeen, and Van Tooren.⁸ Three successive carbon layers of β -SiC, after evaporation of silicon by annealing to 1200°C , collapse into one single layer of carbon atoms with a surface density of 3.67×10^{15} atoms cm^{-2} , very close to the density of a graphite monolayer of 3.80×10^{15} atoms cm^{-2} . This layer of carbon atoms then have only to be displaced over small distances to form a graphite layer. The $6\sqrt{3}\times 6\sqrt{3}$ LEED pattern is due to multiple scattering from the graphite monolayer on top of the Si-terminated β -SiC(111) surface.^{7,8}

In this paper, we present first-principles calculations of the electronic structure of the annealed β -SiC(111) surface based on the above model in order to explain the 6×6 geometry observed in STM images. Because of the large number of atoms involved in a unit cell, calculations were carried out for the graphite monolayer and the Si-terminated β -SiC(111) surface separately. A comparison of the density of states of these two surfaces is shown to produce the 6×6 geometry.

II. EXPERIMENT

A description of our STM with its associated scanning tunneling spectroscopy (STS) system has been given previously.^{6,7} The (111) surfaces of cubic β -SiC monocrystalline films were grown on the Si-terminated (0001) surface of hexagonal α -SiC substrates by the technique of chemical vapor deposition (CVD).⁹ Prior to tunneling, the sample surface was annealed to -1200°C for 1 min to eliminate the surface oxide layer. After this treatment, the surface consistently showed a $6\sqrt{3}\times 6\sqrt{3}$ LEED pattern, in agreement with the results of van Bommel, Crombeen, and Van Tooren.⁸ All STM images of the annealed surface were acquired at a pressure of $\leq 1\times 10^{-10}$ Torr at room temperature.

III. RESULTS

Figure 1 shows voltage-dependent scans of the same region on the annealed β -SiC(111) surface. The surface shows a 6×6 geometry with a unit-cell edge of ~ 19 Å, which is approximately six times the unit-cell edge of 3.1 Å of the β -SiC(111)-(1 \times 1) hulk-terminated surface. The images (a) and (b) of Fig. 1 were taken simultaneously on the same area with the tip biased at $+3.7$ V when scanning from left to right and biased at -3.7 V when scanning from right to left. The hysteresis in the scans was small and had been corrected in the images shown here. The most remarkable feature in these two scans is the occurrence of a contrast reversal. The honeycomb pattern in the filled-state image (a) turns into a centered-hexagon array in the empty-state image (b). The minima of the honeycombs in (a) coincide exactly, as far as the experiment can tell, with the maxima of the centered hexagons in (b). Each honeycomb minimum and each hexagon maximum has a diameter of ~ 12 Å, clearly much larger than the size of a single atom.

Figures 2(a) and 2(b) show filled-state and empty-state images taken with tip biases of $+5$ and -5 V, respectively, on the same area. While the corrugations of filled-

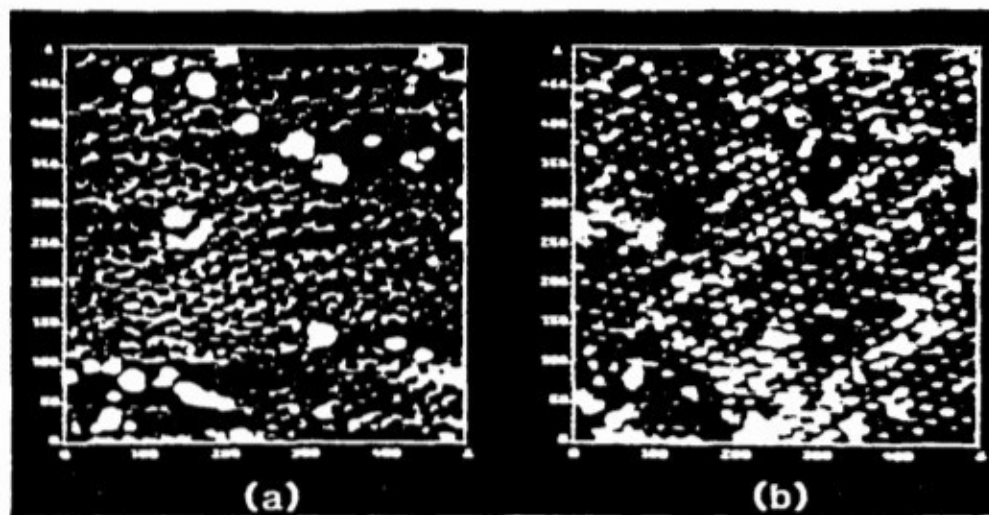


FIG. 1. STM images of the β -SiC(111) surface after annealed at temperature $\sim 1200^\circ\text{C}$. Scan area is $500 \times 500 \text{ \AA}^2$. (Vertically, 1 div = 50 Å; horizontally, 1 div = 100 Å.) Tunneling current = 1 nA. (a) Filled-state image at tip bias $V_t = +3.7 \text{ V}$, and (b) empty-state image at tip bias $V_t = -3.7 \text{ V}$.

state image (a) appear unchanged compared to the corresponding image in Fig. 1(a); the corrugations in the empty-state image (b) have diminished considerably. In Fig. 2, we plot the corrugation as a function of tip bias for images taken at different biases. It is obvious that the corrugations at positive tip bias, i.e., filled-state images, remain relatively constant, while those at negative bias, i.e., empty-state images, decrease as the tip bias decreases. In fact, at tip bias less than -2.5 V , the corrugations almost completely disappear.

IV. DISCUSSION

We have previously reported⁷ the use of STM and STS to show that, upon annealing to 1200°C , a graphite layer is incommensurately grown on top of the Si-terminated β -SiC(111) surface. Our result agrees with previous results obtained by other workers using LEED, Auger electron spectroscopy, x-ray photoemission spectroscopy,

and electron-energy-loss spectroscopy^{1,10-12} on hexagonal α -SiC(0001) surfaces which are, of course, equivalent to the cubic β -SiC(111) surface. In Fig. 4, we have drawn a graphite mesh with a periodicity (or unit-cell edge) of 2.46 \AA over a Si bulk-terminated (1×1) surface of β -SiC(111) with a periodicity of 3.1 \AA . The positions where the top C atoms coincide exactly with the Si atoms underneath are marked with circles and labeled A, B, C, D, E, and F. These positions give rise to the $6\sqrt{3} \times 6\sqrt{3}$ geometry observed by LEED since the unit-cell edges, AE and CE, each have a length of 13 graphite hexagons, i.e., $13 \times 2.46 \text{ \AA}$, which is virtually identical to $6\sqrt{3} \times 3.1 \text{ \AA}$. Around each of the positions A-F, there are three pairs of C and Si atoms at apexes of the dotted triangle lying very close to each other, i.e., within 0.3 \AA laterally. The position G, given by the dotted circle in Fig. 4, does not have any C atoms directly above a Si atom. Six C atoms on the dotted circle, however, are lying very close to six Si atoms. We speculated⁷ that

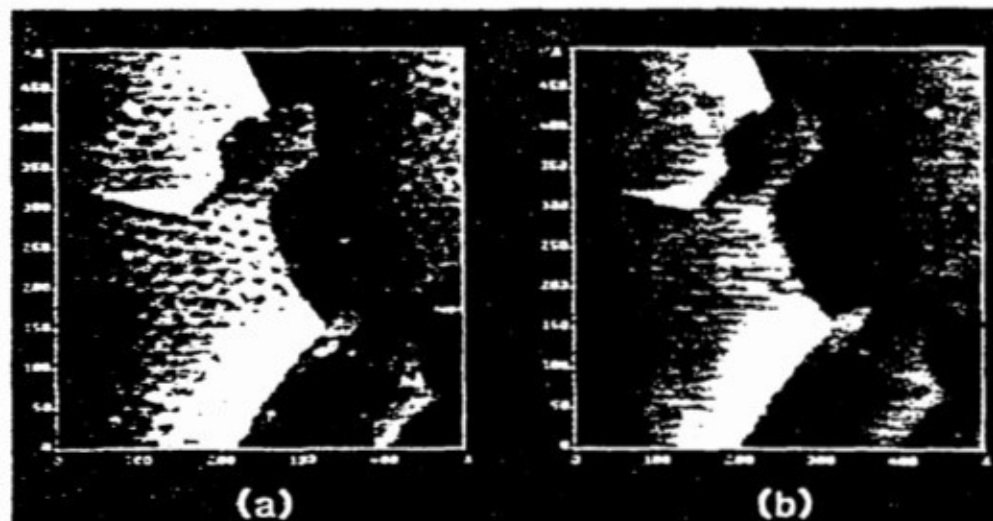


FIG. 2. STM images of the β -SiC(111) surface after annealed at temperature $\sim 1200^\circ\text{C}$. Scan area is $500 \times 500 \text{ \AA}^2$. Tunneling current is 1 nA. (a) Filled-state image at tip bias $V_t = +3 \text{ V}$, and (b) empty-state image at tip bias $V_t = -3 \text{ V}$.

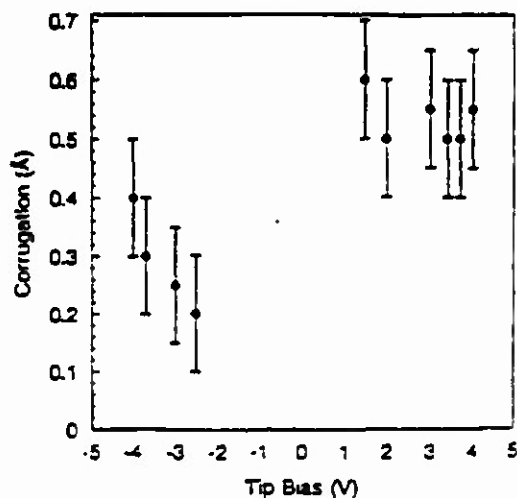


FIG. 3. Z corrugation plotted as a function of tip bias taken from STM images of the β -SiC(111) surface.

ABGF forms the 6×6 geometry observed by STM. To explain the contrast reversal phenomenon as the tip bias is reversed, we need detailed knowledge of the electronic structure of the surface.

To calculate the 6×6 surface directly is beyond the capability of a first-principles method because each unit cell contains hundreds of atoms. Thus, our approach to solve the problem is to model the system separately by a graphite monolayer and a Si-terminated β -SiC(111) surface.

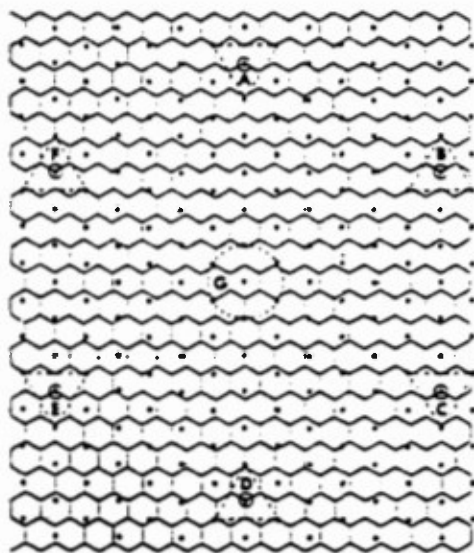


FIG. 4. A model of a graphite monolayer (represented by honeycombs) incommensurately grown on the (1×1) Si-terminated β -SiC(111) surface (represented by dots). The dashed triangles, denoted A, B, C, D, E, and F, indicate positions where the graphite atoms at the centers of triangles coincide exactly with the Si atoms in the second layer, and those graphite atoms at the apexes almost coincide with the Si atoms underneath. The dashed circle, G, outlines positions where the graphite and Si atoms nearly coincide. The unit-cell spacing is 2.46 \AA for graphite and 3.1 \AA for the (1×1) Si-terminated surface.

We use the first-principles pseudofunction (PSF) method¹³ in a local-density approximation (LDA) (Ref. 14) to calculate the electronic structures of the graphite monolayer and the β -SiC(111) surface.

For the β -SiC(111) surface, an isolated eight atomic-layer (or four double-layer) slab model is used. Because of the double-layer nature of β -SiC(111), one surface of the crystal is terminated in Si and the opposite surface is terminated in C. Each C atom on the opposite surface of the slab is attached with a hydrogen atom to saturate the dangling bond in order to prevent charges from transferring back and forth between the two surfaces of the slab, thus making convergence possible. We use the experimental lattice parameter of 4.3596 \AA ,¹⁵ and the hulklike crystal structure for the β -SiC. For the graphite monolayer, we also use an isolated slab model. The lattice parameter is 2.456 \AA as given in the literature.^{16,17} The special k -point scheme of Cunningham¹⁸ for a two-dimensional hexagonal lattice is used to approximate the integration over the first Brillouin zone in calculating the self-consistent charge densities and potential for both cases. We use one special k point for β -SiC and six special k points for graphite.

Calculated energy bands for the β -SiC(111) and the graphite monolayer are shown in Figs. 5 and 6, respectively. In both figures, energies are given relative to the vacuum level. In Fig. 5, there is a very flat half-filled Si dangling-bond energy band around -5 eV inside the fundamental energy gap, giving rise to a very strong peak in the partial density of states of the Si surface atoms as shown in Fig. 7. The calculated energy gap is 1.45 eV , which is about half of the experimental value 2.5 eV .¹⁵ This discrepancy is well known to be the result of a deficiency of the LDA.¹⁹ The Fermi level lies within the dangling-bond state band and is 4.8 eV below the vacuum level, i.e., the work function is 4.8 eV .

For the graphite monolayer, the energy bands shown in Fig. 6 are similar to those of Tatar and Rabi¹⁶ using a modified Korringa-Kohn-Rostoker approach for three-dimensional graphite and also to those of Posternak

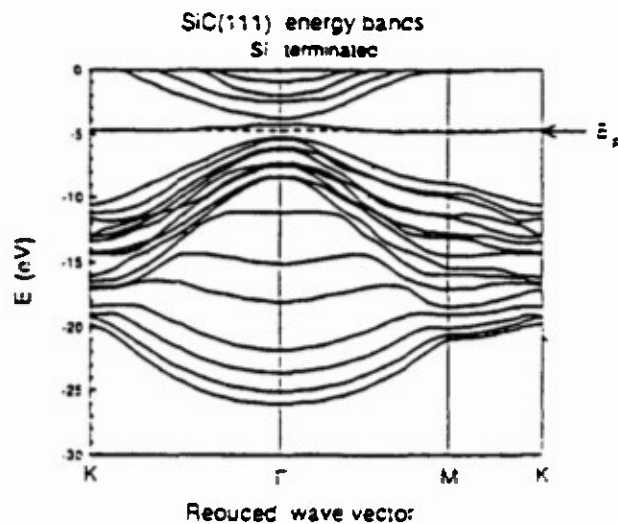


FIG. 5. Calculated energy-band diagram of the Si-terminated surface of β -SiC(111). Dashed line indicates the Fermi level.

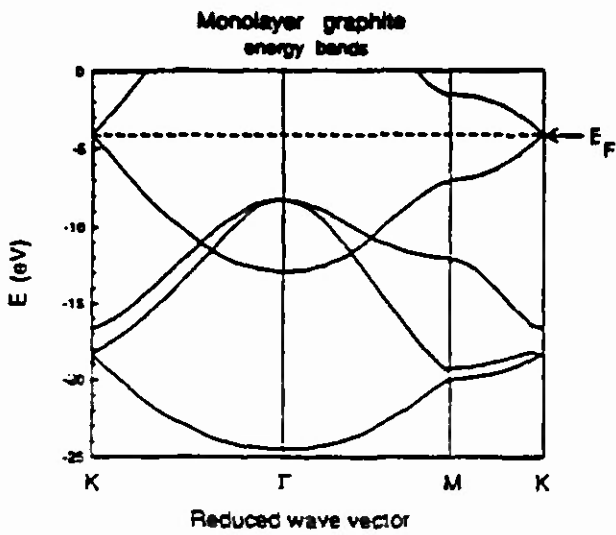


FIG. 6. Calculated energy-band diagram of the graphite monolayer.

et al.²⁰ using the full-potential linearized augmented-plane-wave (FLAPW) method for a graphite monolayer. We obtain a work function for the graphite monolayer compared to 5.02 eV obtained by Posternak et al.²⁰ Previous calculated work functions scatter over a range between 5.0 and 8.0 eV.^{20,21} The experimental work function for bulk graphite is 5.0 eV.¹⁵ The work function for the bulk material is expected to be higher than that for the monolayer because the escaping electron experiences an extra attractive potential from the inner layers despite the fact that the couplings between graphite layers are weak. Thus our calculated work function for the graphite monolayer appears reasonable.

The contributions to the STM images can be approximately divided into two parts, one from the Si dangling-bond states and the other from the graphite electronic states. The Si dangling-bond band is half filled. However, the band and the corresponding density of states are not symmetrical with respect to the Fermi level as indicated in Fig. 5. Referring to Fig. 5, the filled-state part, i.e., the part below the Fermi level (dashed line), is ex-

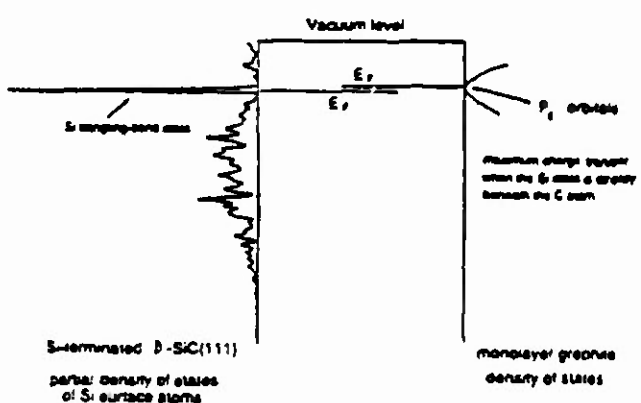


FIG. 7. Calculated partial density of states for the Si-terminated surface of β -SiC(111) and for the graphite monolayer from Ref. 16. The Fermi levels with respect to each other are shown below the vacuum level.

tremely flat and is in the large wave-vector region. In contrast, the empty-state part surrounding the Γ point has a more pronounced curvature, i.e., larger energy spread, and has smaller wave vectors. Thus the empty states are more delocalized and the corresponding density of states is much smaller than that for the filled states. Because of this, one expects the contribution of the Si dangling-bond states to be larger for filled-state images (i.e., positive tip bias) than for empty-state images (negative tip bias).

Since the work function for the graphite monolayer is smaller than that for the Si-terminated β -SiC(111), there is a net charge transfer from the graphite to the β -SiC. The graphite Fermi level is located at the π band, which is composed solely of p_z orbitals; here, z is the coordinate normal to the surface. When there is a Si atom directly beneath or close to a C atom in the graphite layer, the charge transfer from the C atom to underneath the Si atom will be maximum. Otherwise, the charge transfer will be small due to the highly directional p_z orbital. We write $\rho_1(E)$ for the density of states of those C atoms which have a Si atom directly underneath or close to them, i.e., C atoms in regions A-G in Fig. 4, and $\rho_2(E)$ for the density of all other C atoms. The density of states for bulk graphite has been given by Tatar and Rabi.¹⁶ Since the energy bands of the graphite monolayer are similar to those of bulk graphite, the density of states for them will be similar. Within about 2.5 eV of the Fermi level, the density of states is approximately parabolic,¹⁶ which is shown in Fig. 8. Thus

$$\rho_2(E) = K(E - E_F)^2, \tag{1}$$

where K is a proportionality constant.

For those C atoms with a Si atom underneath or in close proximity, charge transfer from C to Si atoms will shift the density-of-states curve downwards by an amount δ as shown in Fig. 8, resulting in an attractive electrostat-

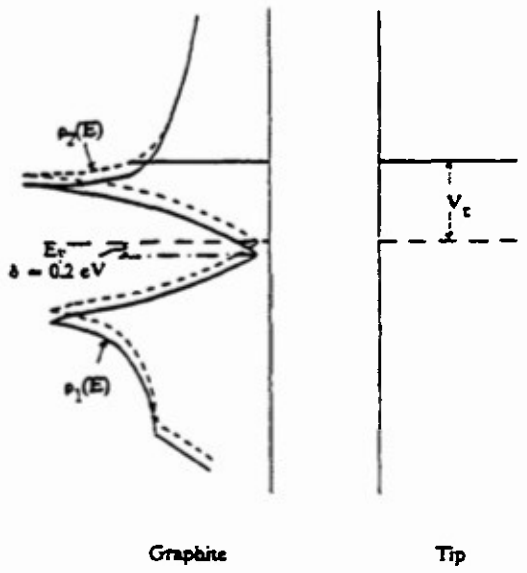


FIG. 8. Shift in the density of states of the graphite monolayer (Ref. 16) as a result of charge transfer. The number of states samples by different tip biases is also shown.

ic potential. δ has a positive value in energy units. Then

$$\rho_1(E) \approx K(E - E_F + \delta)^2. \quad (2)$$

For tip bias V_t , let $N_1(E_F, V_t)$ and $N_2(E_F, V_t)$ be the numbers of states between E_F and $E_F - eV_t$ for the kinds of C atoms mentioned earlier. Let ΔN be the difference in the number of states sampled by STM from the two kinds of C atoms on the surface, which in turn gives rise to the contrast observed in Figs. 1 and 2. Hence

$$\Delta N = N_1(E_F, V_t) - N_2(E_F, V_t). \quad (3)$$

We write ΔN^+ for $V_t > 0$ or positive tip bias (sampling filled states), and ΔN^- for $V_t < 0$ or negative tip bias (sampling empty states). From Eqs. (1)–(3), we now have

$$\Delta N^+ = \int_{E_F - eV_t}^{E_F} K \rho_1(E) dE - \int_{E_F - eV_t}^{E_F} K \rho_2(E) dE \quad (4)$$

giving

$$\Delta N^+ \approx -K[(eV_t)^2 \delta - (eV_t) \delta^2] \quad (5)$$

or

$$\Delta N^+ \approx -Ke^2 V_t^2 \delta.$$

Similarly,

$$\Delta N^- = \int_{E_F}^{E_F - e|V_t|} K \rho_1(E) dE - \int_{E_F}^{E_F - e|V_t|} K \rho_2(E) dE, \quad (6)$$

$$\Delta N^- \approx Ke^2 V_t^2 \delta. \quad (7)$$

The opposite signs in Eqs. (5) and (7) explain the contrast reversal observed in the (a) and (b) images in Figs. 1 and 2.

In Eq. (7) for empty-state images, the contrast has a V_t^2 dependence, which means the contrast is large for large negative tip bias, but decreases rapidly as the bias decreases. This may explain the corrugation dependence shown in Fig. 3, i.e., the empty-state images show little corrugation for small negative tip bias, and the corruga-

tion only becomes pronounced at large biases. Such a dependence is not observed for filled-state images because of the influence of the Si dangling-bond states.

As we have discussed earlier, the empty Si dangling-bond states are more delocalized or diffused. Their contribution relative to that of graphite states includes a geometric factor of roughly $e^{-2d\sqrt{\phi}}$, where ϕ is the work function in Ry and d is the distance between the graphite layer and the Si surface layer in Bohr radius. This factor has an order of 10^{-2} , which implies a negligible contribution to the empty-state images. On the other hand, for positive tip biases measuring the filled states, the very strong localized Si dangling-bond states should be able to compensate for the deficiency caused by the geometric factor and contribute significantly to the filled-state images. This may be the reason why the corrugations in the filled-state images in Figs. 1 and 2 are insensitive to changes in tip bias.

V. CONCLUSIONS

The discrepancy between the 6×6 STM geometry and the $6\sqrt{3} \times 6\sqrt{3}$ LEED pattern for the β -SiC(111) surface can be explained by an incommensurate graphite monolayer grown on the Si-terminated β -SiC(111) surface during the annealing process. The contrast reversal phenomenon observed in the STM images at opposite tip biases can be explained by the different electronic contributions from graphite states of those C atoms with Si atoms directly (or almost directly) underneath and those without. The Si dangling-bond states contribute significantly to the corrugations observed in the filled-state images.

ACKNOWLEDGMENTS

We thank Y. C. Wang and R. F. Davis of North Carolina State University for providing the β -SiC(111) single crystals. We also thank U. Knipping for improvements in the STM imaging and spectroscopy software. This work was supported by the U.S. Army Research Office under Contracts DAAL 03-88-K-0098 and DAAL 03-91-G-0054.

¹G. Binnig, H. Rohrer, Ch. Gerber, and E. Weibel, *Phys. Rev. Lett.* **50**, 120 (1982).

²R. J. Hamers and J. E. Demuth, *Phys. Rev. Lett.* **60**, 2527 (1988).

³J. A. Stroscio, R. M. Feenstra, D. M. News, and A. P. Fein, *J. Vac. Sci. Technol. A* **6**, 499 (1988).

⁴R. J. Wilson and S. Chiang, *Phys. Rev. Lett.* **58**, 369 (1987).

⁵E. J. van Loenen, J. E. Demuth, R. P. Tromp, and R. J. Hamers, *Phys. Rev. Lett.* **58**, 375 (1987).

⁶C. S. Chang, N. J. Zheng, I. S. T. Tsong, Y. C. Wang, and R. F. Davis, *J. Vac. Sci. Technol. B* **9**, 681 (1991).

⁷C. S. Chang, I. S. T. Tsong, Y. C. Wang, and R. F. Davis, *Surf. Sci.* **256**, 354 (1991).

⁸A. J. van Bommel, J. E. Crombeen, and A. van Tooren, *Surf. Sci.* **48**, 463 (1975).

⁹H. S. Kong, J. T. Glass, and R. F. Davis, *J. Mater. Res.* **4**, 204 (1989).

¹⁰R. Kaplan, *Surf. Sci.* **215**, 111 (1989).

¹¹L. Muehlhoff, W. J. Choyke, M. J. Bozack, and J. T. Yates, Jr., *J. Appl. Phys.* **60**, 2842 (1986).

¹²K. Miyosi and D. H. Buckley, *Appl. Surf. Sci.* **10**, 357 (1982).

¹³R. V. Kasowski, M.-H. Tsai, T. N. Rhodin, and D. D. Chambliss, *Phys. Rev. B* **34**, 2656 (1986).

¹⁴L. Hedin and B. I. Lundqvist, *J. Phys. C* **4**, 2064 (1971).

¹⁵*Handbook of Chemistry and Physics*, 71st ed., edited by D. R. Lide (CRC, Boca Raton, FL, 1990–1991); B. Robneux, R. Faure, and J. P. Dussauley, *C. R. Acad. Sci. Ser. B* **278**(14), 659 (1974).

¹⁶R. C. Tatar and S. Rabii, *Phys. Rev. B* **25**, 4126 (1982).

¹⁷D. Sands, *Introduction to Crystallography* (Benjamin-

Cummings, Reading, MA, 1969).

¹⁸S. L. Cunningham, *Phys. Rev. B* 10, 4988 (1974).

¹⁹M. S. Hybertsen and S. G. Louie, *Phys. Rev. B* 34, 5390 (1986).

²⁰M. Posternak, A. Baldereschi, A. J. Freeman, E. Wimmer, and M. Weinert, *Phys. Rev. Lett.* 50, 761 (1983).

²¹A. Zunger, *Phys. Rev. B* 17, 626 (1978), and references therein.

Relaxation of the ZnTe and CuCl (110) surfaces

M.-H. Tsai, W.-M. Hu, John D. Dow, and O. F. Sankey

Department of Physics and Astronomy, Arizona State University, Tempe, Arizona 85287-1504

(Received 1 October 1991; accepted 31 December 1991)

Ab initio molecular dynamics simulations of the ZnTe and CuCl (110) surfaces are employed to study surface atomic relaxation. We believe that these are the first such computations for heteropolar semiconductors, and for their surfaces in particular. The molecular dynamics follows the Sankey-Niklewski method, and electrostatic interactions are incorporated using Ewald's scheme for Gaussian atomic charge distributions. Hence the electrons are treated in the local-density approximation, forces are computed using the Hellmann-Feynman method, and atoms move to equilibrium according to Newton's laws. Using "dynamical quenching," we allow the "ideal" surfaces to relax according to these laws of physics and then address a controversy concerning whether Coulomb forces can play a significant role in determining the (110) zinc blende surface relaxation: Coulomb effects are not negligible for ZnTe (110) and are as dominant as covalent effects for CuCl (110). They reduce the (almost rigid) bond rotation angle ω_1 due to movement of the anions up out of the (110) surface by about 6° for ZnTe, and cause the CuCl anion rotation angle to be nearly zero.

1. INTRODUCTION

Low-energy electron diffraction (LEED) analysis is a very useful tool for determining the atomic positions at a surface. This analysis, as currently practiced,¹ uses various methodologies to determine which atomic geometry yields electron diffraction intensities that best fit data. Simplified models of solids are usually used to predict these intensities, which are rather difficult to calculate. One such model divides the solid into ion cores and a uniformly distributed electron gas;¹ the ion cores are singly ionized atoms, independent of the ionicities of the materials. Using this model, Duke *et al.* have done LEED analyses of the ZnTe (110) surface² and concluded that the relaxation of this surface is as large as that of GaAs, with a surface bond-rotation angle ω_1 of 30° . Based on these and similar analyses for other zinc blende semiconductors, those authors have hypothesized that (110) surfaces of all zinc blende semiconductors have virtually the same surface relaxation, a nearly rigid rotation of the anions up out of the surface through an *ionicity-independent* angle $\omega_1 \approx 29^\circ$. It is difficult to understand how the relaxation, which for low-ionicity materials is dominated by covalent forces, can be independent of ionicity, since the Coulomb forces by the subsurface cations should pull the surface anions back down toward the surface plane; for large enough ionicity, those forces should largely cancel the relaxation due to covalent forces.

The present paper addresses the issue of whether or not such a *universal* (110) surface relaxation is to be expected theoretically, using a first-principles local-density approximation theory that neither divides up the solid arbitrarily nor replaces the actual valence charge distribution with uniform charge densities. Furthermore, the present theory allows the surface to relax according to Newton's laws, with the interatomic forces calculated quantum mechanically. No *a priori* model of the ultimate relaxation geometry is fed into the calculations; the equations of motion, as implemented by our formalism, determine the relaxation entirely.

Most of the data analyses which support the universal rigid rotation model have involved low-ionicity semiconductors such as GaAs. ZnTe is a notable exception, having a relatively large ionicity and a relatively large (longitudinal) effective charge.³ To date, LEED analyses of the CuCl (110) surface have not been presented, to our knowledge, but this semiconductor has one of the largest ionicities of all of the zinc blendes. The Coulomb interactions of effective charges should tend to suppress surface relaxation, provided surface atoms have comparable effective charges to those of bulk atoms. The above-surface, negatively charged, relaxed anions are attracted back toward the surface by near-surface cations. The pseudofunction theory⁴ included these Coulomb effects, as well as the covalent physics of most other models, and concluded that ω_1 for ZnTe (110) should be about 5° smaller than for GaAs (110), almost entirely due to Coulomb interactions. Thus there is a controversy between Duke *et al.* on the one hand, who propose that the reconstruction angle ω_1 is virtually independent of ionicity and Tsai *et al.* on the other who predict an ionicity dependence. Duke *et al.* base their arguments on analyses of data with theory that does not handle Coulomb effects. Tsai *et al.* have purely theoretical arguments. The theories predict virtually the same relaxation for GaAs, differ somewhat for ZnTe, and differ greatly for CuCl, where the ionicity is sufficiently large that Tsai *et al.* predict that the Coulomb forces inhibit relaxation, leading to a value of ω_1 near zero.

Intermediate between the theories of Tsai *et al.* and Duke *et al.* is pioneering work by Chadi,⁵ who calculated the surface atomic geometries using a total energy method based on (bulk) tight-binding parameters and phenomenological ideas about ionicity. Chadi concluded that the rotation angles were virtually independent of ionicity, although the heights that the surface anions assume above the surface decrease with ionicity.

Neither the Tsai *et al.* theory nor the Duke *et al.* work actually predicts the positions of surface atoms; rather both

assume a surface geometry. Then Tsai *et al.* predict its electronic properties, including total energy, to verify that the assumed geometry is correct, namely that it has a (locally) minimum total energy. In most of the work of Duke *et al.*,^{1,2} the assumed geometries are varied to optimize agreement with selected data, such as LEED intensities. As a rule, only the surface and one to three subsurface layers are allowed to relax in the models involved in LEED analyses. Given this situation, we thought it might be instructive to allow the surface to relax according to the laws of physics, with no preconceived model of how the relaxation occurs. Our approach uses a "solid" that is six atomic layers thick (and so should contain all of the physics of the previous models), and employs the well-established local-density approximation in a first-principles Newtonian molecular dynamics.

II. OUTLINE OF METHOD

Our approach is based on the very-efficient, first-principles, real-space method of Sankey and Niklewski for molecular dynamics simulations of covalent materials.⁶ Forces on atoms are computed using the quantum-mechanical local-density approximation in a tight-binding-like formalism, and the atoms move in response to these forces according to Newton's laws of motion. This method has worked well for various systems of C and Si atoms.⁶⁻⁹ In the original method, a neutral-atom approximation is used to simplify the formalism and to enhance the efficiency of computation. This approximation, however, also limits the application of the method to materials with small effective charges.

In the present work, we have extended the method to more ionic systems by incorporating Ewald's technique¹⁰ to calculate the long-ranged Coulomb potentials associated with non-neutral atoms. This scheme, which is presented in detail elsewhere,¹¹ is computationally very fast, and so we are able to extend the multicenter tight-binding molecular dynamics method to a wide range of materials, without trading off much computational efficiency.

The essence of the new treatment of charge transfer is that a Gaussian charge distribution centered on each atomic site, with its charge chosen to neutralize the atomic charge, is both added and subtracted. Then the atoms with their neutralizing Gaussian charges are treated as the neutral pseudoatoms of the Sankey-Niklewski method, and the negative of the array of neutralizing Gaussian charges is treated using Ewald's method. (Note that overall the array of Gaussian charges is neutral.) The numbers of *s* and *p* valence electrons, as defined by the occupation numbers of *s* and *p* orbitals for a given atom, are determined self-consistently, and, in general, are nonintegers. The detailed algebra of these modifications of the neutral-atom theory are given in Ref. 11.

The ZnTe (110) surface is modeled by a six layer slab repeated-slab model (i.e., a super-cell model) with periodic boundary conditions in three dimensions. The vacuum region between adjacent slabs is 8.5 Å thick. The ideal surface plane corresponds to $z = 0$, and the relaxed anions lie in the upper half-plane for ZnTe ($\omega_1 > 0$). The observed

lattice constant of bulk ZnTe, 6.101 Å,¹² is used to determine the reference lattice and to define basis and reciprocal-lattice vectors. (We have tested that an adjustment of the lattice constant by 0.1 Å does not significantly alter the surface-bond rotation.) For CuCl, we treat the Cu *d* electrons as core electrons rather than valence electrons, and this causes the theoretical bulk lattice constant to differ somewhat from the experimental one. Hence, we use the theoretical value, 4.70 Å here, in order to be completely consistent theoretically.¹³ The masses of atoms in the bottom surface of the slab are set to huge numbers, so that, for all practical purposes, these atoms are motionless and are regarded as fixed bulk atoms. All atoms in other layers have atomic masses (66.38, 127.60, 63.546, and 35.453) a.u. for Zn, Te, Cu, and Cl, respectively. The unit cell contains twelve atoms, e.g., one Zn and one Te atom per layer. We use *s* and *p* orbitals centered on all atoms and treat the *d* orbital of Cu as a core electron that is contained in the pseudopotential and does not participate in the molecular dynamics. Molecular dynamics simulations are started assuming the ideal, unrelaxed zinc blende (110) surface. Movements of all atoms are governed by the total forces acting on them. During the simulation, the velocities of all atoms are quenched (set to zero) when the instantaneous temperature for a given time step is smaller than for the previous time step. This means that, overall, the atoms decelerate. Each time step is 2.074 fs long. The simulation is terminated when all atomic positions stabilize. For each time step, the charges or the occupation number of the valence *s* and *p* orbitals on all atoms are determined self-consistently, within a tolerance of 0.01 electrons. The self-consistency in charge is more readily achieved with each successive time-step.

III. RESULTS

Using the original *zero-charge-transfer* method of Sankey and Niklewski,⁶ we obtain $\omega_1 = 31^\circ$ and a second-layer bond-rotation angle $\omega_2 = 5^\circ$ for ZnTe (110). The corresponding results for CuCl are $\omega_1 = +31^\circ$ and $\omega_2 = -7^\circ$. The results for ZnTe and CuCl are similar to the well-known surface relaxation of GaAs(110): $\omega_1 = 30.6^\circ$ and $\omega_2 = -6.2^\circ$ by this method. GaAs has a small effective charge, and so is close to the purely covalent limit. As stated previously, the Sankey-Niklewski method assumes that all atoms are neutral and there is no long-ranged Coulomb potential. Thus these zero-charge-transfer results can be regarded as the covalent limit in which the surface anions rise up out of the surface and the cations descend toward the bulk, such that the surface-bond rotates by about $29^\circ \pm 2^\circ$ (the commonly accepted value of ω_1).

With the inclusion of charge-transfer and long-ranged Coulomb forces, we find that the relaxation of the ZnTe (110) surfaces still can be described as a surface bond rotation and a second layer counter rotation. (For CuCl, a similar model, but with more bond contraction and distortion, is necessary.) Hence the model is described by the two angles ω_1 and ω_2 , and the *z* displacements of anions and cations. (See Figs. 1 and 2.) The displacements of the

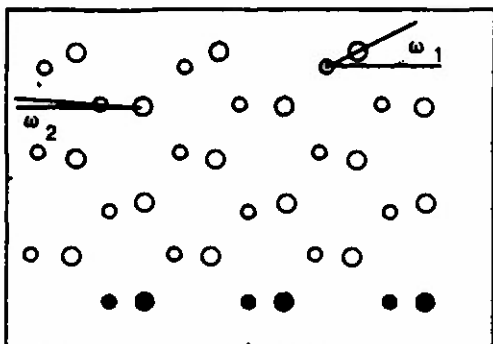


FIG. 1. The side view of the relaxed zinc blende (110) surface. Smaller and larger circles correspond to cations and anions, respectively. The angle between the plane $z=0$ (the unrelaxed surface) and the surface anions is ω_1 . The dark circles are essentially infinitely massive in the present model.

near-surface atoms predicted by the simulations are given in Tables I and II for ZnTe and CuCl, respectively.

In the case of ZnTe, the predicted bond-rotation angle ω_1 with charge transfer is significantly reduced in comparison with both GaAs and zero-charge-transfer ZnTe, being $\omega_1 = 24.6^\circ$; in this case we have $\omega_2 = 4.6^\circ$. Hence ω_1 is about 6° smaller than obtained for neutral atoms with zero-charge transfer. (This compares favorably with a corresponding difference of 5° obtained using the pseudofunction method, fixing the bond lengths, and allowing only the top layer of atoms to relax.)⁴

For CuCl, there is almost no surface bond rotation: the theory predicts $\omega_1 = +3.6^\circ$ and $\omega_2 = +6.2^\circ$. The molecular dynamics calculations that we have executed assume that the Cu d electrons are part of the core. Hence the coupling of the Cu d electrons to the sp valence band has been neglected.

In order to determine that this neglect of d - sp coupling is a reasonable approximation, we have done pseudofunction calculations,¹⁴ which do account for the coupling, for a four-layer isolated slab. The pseudofunction calculations are computationally intensive, so the only relaxation that is allowed is a rigid rotation of the surface layer through an angle ω_1 . When we do these calculations with the d elec-

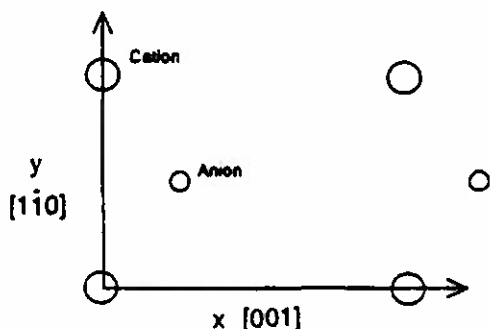


FIG. 2. Illustrates the coordinate system with x positive in the [001] direction, y positive in the [110] direction, and z positive normal to the unrelaxed (110) surface.

TABLE I. Calculated atomic displacement ΔR (in Å) with respect to the ideal truncated bulk geometry, as calculated for the ZnTe (110) surface: $\Delta R = (\Delta x, \Delta y, \Delta z)$ where z is normal to the surface, x is in the [001] direction, and y is in the [110] direction. Coordinates for fourth and deeper layers should be viewed as unreliable, because the model fixes the bottom (sixth) layer.

Layer, atom	ΔR
First, Zn	(+0.27, -0.04, -0.27)
First, Te	(+0.13, -0.02, +0.37)
Second, Zn	(-0.38, +0.01, +0.19)
Second, Te	(-0.05, +0.04, +0.10)
Third, Zn	(+0.00, +0.00, +0.20)
Third, Te	(+0.08, +0.00, -0.01)
Fourth, Zn	(-0.01, +0.00, -0.21)
Fourth, Te	(+0.05, +0.00, +0.13)
Fifth, Zn	(-0.24, +0.00, +0.02)
Fifth, Te	(-0.11, +0.00, -0.08)
Sixth, Zn	(+0.00, +0.00, +0.00)
Sixth, Te	(+0.00, +0.00, +0.00)

trons constrained to the core, we find $\omega_1 = -0.13^\circ$, only 3.7° different from the comparable molecular dynamics result. When we treat the Cu d electrons as valence electrons and let them couple to Cl's s and p electrons, we find $\omega_1 = +1.44^\circ$, comparable with both the molecular dynamics and the pseudofunction results for d electrons in the Cu core. Thus we conclude that our treatment of the Cu d electrons introduces an insignificant uncertainty to the result for ω_1 of about 1.6° .

Tables I and II give our predicted relaxed-surface coordinates for ZnTe (110) and CuCl (110). The final configurations were obtained by the surface atoms successively distorting and accelerating from the "ideal" surface in time intervals of 2.074 fs. After a time interval in which the kinetic energy of the surface increases, the surface is "cooled" by having all its atomic velocities set to zero. While this is a kinder and gentler way of relaxing to equilibrium than cleavage, it nevertheless should provide a good model of the (110) surface's equilibrium state. Therefore, we believe that the qualitative conclusion that ω_1 de-

TABLE II. Calculated atomic displacement ΔR (in Å) with respect to the ideal truncated bulk geometry, as calculated for the CuCl (110) surface: $\Delta R = (\Delta x, \Delta y, \Delta z)$ where z is normal to the surface, x is in the [001] direction, and y is in the [110] direction.

Layer, atom	ΔR
First, Cu	(+0.32, -0.12, -0.21)
First, Cl	(-0.21, +0.17, -0.17)
Second, Cu	(+0.16, +0.10, +0.13)
Second, Cl	(-0.34, -0.20, -0.05)
Third, Cu	(+0.21, -0.11, +0.10)
Third, Cl	(-0.28, +0.19, -0.15)
Fourth, Cu	(+0.24, +0.13, +0.05)
Fourth, Cl	(-0.30, -0.18, -0.07)
Fifth, Cu	(+0.19, +0.13, -0.14)
Fifth, Cl	(-0.26, -0.20, -0.15)
Sixth, Cu	(+0.00, +0.00, +0.00)
Sixth, Cl	(+0.00, +0.00, +0.00)

creases significantly with ionicity must be correct. We believe that only if the local-density approximation for computing atomic forces is inadequate for computing charge transfer,¹⁵ or if our slab is too thin, could these conclusions be reversed. Since the local-density approximation has a long history of being adequate, and because we have studied the dependence on super-cell size (See Appendix), we think that future progress on this problem is likely to come from reanalysis of LEED data and from LEED experiments on CuCl (110).

From our results, the electrostatic effects on zinc blende (110) surface relaxation are clearly demonstrated. Our results agree with previous calculations of Tsai *et al.* using the first-principles pseudofunction method, and disagree with the analyses of LEED intensities.

IV. SUMMARY

In summary, using an improved *ab initio* multicenter real-space tight-binding-like method of molecular dynamics simulations that allows charge transfer among atoms, we found that the relaxations of the ZnTe (110) and CuCl (110) surfaces are significantly smaller than that of GaAs (110), due to Coulomb interactions between atoms. In the case of CuCl the effect was so dramatic that there was almost no relaxation at all. Our results imply that a complete understanding of the zinc blende (110) surfaces requires an adequate treatment of charge transfer.

ACKNOWLEDGMENT

The authors are grateful to the Army Research Office for their generous support (Contract No. DAAL03-91-G-0054).

APPENDIX

First principles molecular dynamics calculations of the sort presented here are computationally intensive, and hence demand a limited size for the super cell. We have used a rather large slab with six layers, essentially fixing the positions of the atoms in the bottom (sixth) layer. If the atomic displacements from lattice sites in the fifth layer were nearly zero, we could be completely confident that our results had fully converged with respect to slab size. However the atomic displacements in the third to fifth layers are significant (see Table I)—a reflection of the fact that elastic forces are long ranged, and a source of concern that the slab may be too thin.

TABLE III. Calculated differences in atomic displacements ΔR (in Å) ZnTe (110) surface for a six-layer model minus a five-layer model: $\Delta R = \delta(\Delta x, \Delta y, \Delta z)$ where x is normal to the surface, x is in the [001] direction and y is in the [1 $\bar{1}$ 0] direction.

Layer, atom	ΔR
First, Zn	(+ 0.02, + 0.05, + 0.05)
First, Te	(+ 0.07, + 0.05, + 0.03)
Second, Zn	(- 0.03, - 0.06, - 0.02)
Second, Te	(+ 0.01, + 0.05, + 0.06)

To address the dependence on slab size within the stringent limitations imposed on us by available computational resources, we computed a five-layer model of ZnTe (110) and compared it with the corresponding six-layer model.¹³ The differences in the angles ω_1 and ω_2 were -1.4° and -3° , respectively. The corresponding differences in displacements are given in Table III, and are a good indication of uncertainties in the calculations.

- ¹ See, for example, W. K. Ford, C. B. Duke, and A. Paton, *Surf. Sci.* **115**, 195 (1982).
- ² C. B. Duke, A. Paton, and A. Kahn, *J. Vac. Sci. Technol. A* **1**, 672 (1983).
- ³ G. Lucovsky, R. M. Martin, and E. Burstein, *Phys. Rev. B* **4**, 1367 (1971).
- ⁴ M.-H. Tsai, J. D. Dow, R.-P. Wang, and R. V. Kasowski, *Phys. Rev. B* **40**, 3810 (1989).
- ⁵ D. J. Chadi, *Phys. Rev. B* **19**, 2074 (1979).
- ⁶ O. F. Sankey and D. J. Niklewski, *Phys. Rev. B* **40**, 3979 (1989).
- ⁷ O. F. Sankey, D. J. Niklewski, D. A. Drabold, and J. D. Dow, *Phys. Rev. B* **41**, 12750 (1990).
- ⁸ G. B. Adams and O. F. Sankey, *Phys. Rev. Lett.* **67**, 867 (1991).
- ⁹ G. B. Adams, J. B. Page, O. F. Sankey, K. Sinha, and J. Menendez, *Phys. Rev. B* **44**, 4052 (1991).
- ¹⁰ P. P. Ewald, *Ann. Phys.* **64**, 253 (1921); *Göttinger Nachr. Math. Phys. Kl. II* **3**, 55 (1937).
- ¹¹ M.-H. Tsai, O. F. Sankey, and J. D. Dow (to be published).
- ¹² *CRC Handbook of Chemistry and Physics*, edited by D. R. Lide, 71st ed. (Chemical Rubber, Boca Raton, FL, 1990-91).
- ¹³ With the exception of Table III, the parameter r_c of the Sankey-Niklewski model is 2.38 Å for Cu, 3.24 Å for Te, 2.78 Å for Zn, and 2.65 Å for Cl. For Table III, we used $r_c = 2.82$ Å for Zn and 3.06 Å for Te. The parameter r_c is chosen mostly for convenience, provided a reasonable charge transfer can be obtained, as determined by q/ϵ_0 , where q is the longitudinal effective charge and ϵ_0 is the static dielectric constant. The bulk lattice constant of CuCl is 3.4057 Å.
- ¹⁴ R. V. Kasowski, M.-H. Tsai, T. N. Rhodin, and D. D. Chambliss, *Phys. Rev. B* **34**, 2656 (1986).
- ¹⁵ The charge transfer obtained here is essentially the same as obtained in Ref. 4. We did note some sensitivity of the calculated charge transfer to the cutoff radius r_c . Hence we believe that the charge transfer of Ref. 4 is the characteristic value to be expected from local-density theory, independent of how that theory is implemented computationally.

FABRICATION OF QUANTUM DOTS ON THE InSb (110) SURFACE

Yong Liang

Laboratory for Research in the Structure of Matter
University of Pennsylvania, Philadelphia, PA 19104

and

William E. Packard and John D. Dow

Department of Physics and Astronomy
Arizona State University, Tempe, AZ 85287

(Received 11 March 1992)

Using a scanning tunneling microscope, quantum dots with diameters of order 25 Å have been fabricated on the cleaved InSb(110) surface in UHV. Both In and Sb atoms were clearly resolved on the cleaved surface.

Scanning tunneling microscopes (STM's) present the opportunity not only to image a semiconductor surface with unprecedented resolution but also to controllably alter the surface on the Angstrom scale, as a result of the tip-surface interaction. Becker et al. demonstrated that single atoms could be manipulated on the Ge(111) surface with a single voltage pulse [1]. A number of authors [2] have "machined" various surfaces on the nanometer scale, either by crashing the STM tip into the surface, by applying voltage pulses, or by local heating -- with experiments performed in air, under liquids, or in ultra-high vacuum. In this paper we present some of the first [3] STM images of the InSb(110) surface under ultra-high vacuum and we show how quantum dots can be controllably engraved in the surface.

We employed a Pachyderm-4 sculpted STM [4], which is machined almost in its entirety from a single block of stainless steel and hence has unusual vibrational stability. With this STM, we obtained the images of Fig. 1 and Fig. 2 by scanning the InSb(110) surface. This surface was cleaved in 10^{-11} Torr vacuum, and the images were taken with a tunneling current of ≈ 120 pA. Fig. 1 was taken with a negative sample bias of -0.2 V, and so is sensitive to the electronically occupied, Sb-like states of the valence band. The prominent features of the image are Sb atoms, spaced by the accepted lattice constants (assuming a 29° Rigid Rotation Model [5] of the surface relaxation). The number of visible defects in this region of the surface is about one per $\approx 10^3$ atoms.

Fig. 2 shows InSb before and after a quantum-dot hole is fabricated on its (110) surface. Positive sample bias of +0.3 V produced the

images of Fig. 2a and 2b, which are sensitive to electronically empty, In-derived states. Negative bias of -0.3 V, yielded Fig. 2c.

By positioning the STM tip over a spot for $\approx 10^{-6}$ s we formed quantum dots, such as those of Figs. 2b and 2c. The positions of the dots were easily controllable. The perfect InSb(110)

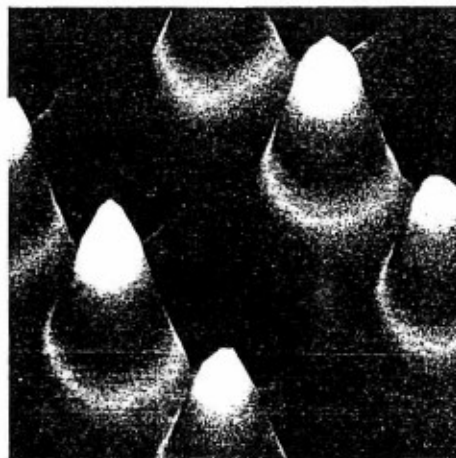


Fig. 1. STM image of InSb(110) with atomic resolution. The surface was cleaved in ultra-high vacuum (10^{-11} torr range) and imaged at -0.2 V sample bias with 120 pA tunneling current. With negative bias the Sb atoms are prominent and the In atoms are almost invisible. The data were Fourier filtered.

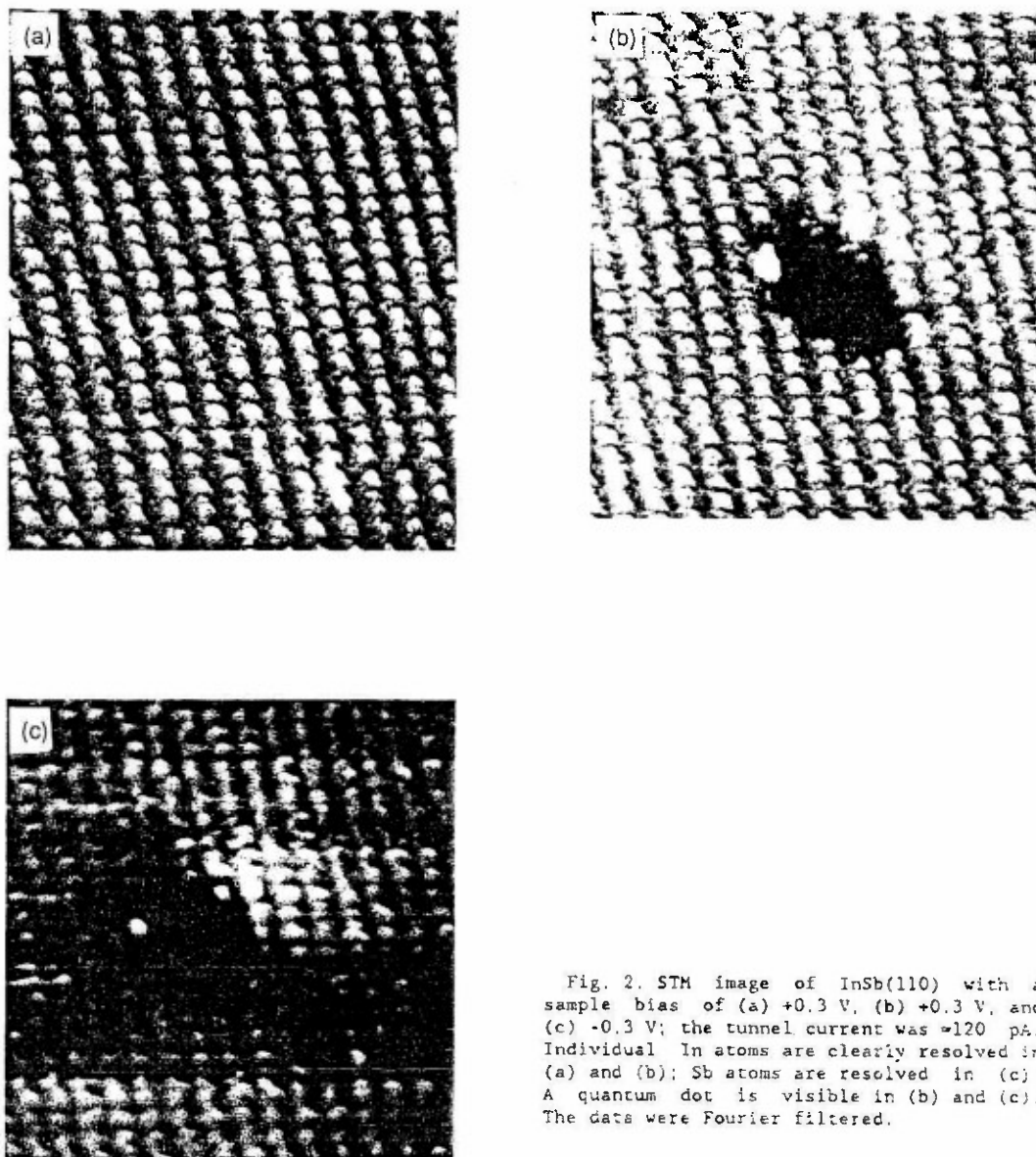


Fig. 2. STM image of InSb(110) with a sample bias of (a) +0.3 V, (b) +0.3 V, and (c) -0.3 V; the tunnel current was ≈ 120 pA. Individual In atoms are clearly resolved in (a) and (b); Sb atoms are resolved in (c). A quantum dot is visible in (b) and (c). The data were Fourier filtered.

surface was more susceptible to disruption by the STM tip than other surfaces we have studied [2,6], and so preservation of the perfect surface required rapid scanning, while the formation of quantum dots was almost effortless. The diameter of the dot in Fig. 2 is about ≈ 25 Å as can be deduced by recognizing that the Sb atoms of Fig. 2b exhibit a rectangular surface unit cell of $6.5 \text{ Å} \times 4.6 \text{ Å}$. Close inspection of Figs. 2b and 2c reveals images of individual Sb and In atoms.

The quantum dot is a small surface void, with a depth of one or two atoms, 2 Å to 4 Å, as determined by scanning in the dot. The size of

the voids can be increased by holding the tip fixed for a longer time or by scanning over a very small area.

These results demonstrate that Angstrom-scale STM lithography of InSb(110) surfaces will be feasible, and that it might be possible, if the electronic structures of the quantum dots are favorable, to fabricate Angstrom-scale memory bits on this surface.

Acknowledgment -- We are grateful to the U.S. Army Research Office for their support of this work (Contract No. DAAL03-87-K-0112). We have also benefited from stimulating discussions of

STM design with R. Jaklevic, W. Kaiser, and S. L. Tang, and we thank B. Swartzentruber for a copy of his STM software. Much of this research was performed when all three authors were at the University of Notre Dame. We thank Prof. M. A. Bowen for being acting editor for this manuscript.

REFERENCES

- [1] R. S. Becker, J. A. Golovchenko, & B. S. Swartzentruber, *Nature* **325**, 419 (1987).
- [2] W. E. Packard, Y. Liang, N. Dai, J. D. Dow, R. Nicolaides, R. C. Jaklevic, & W. J. Kaiser, *J. Microscopy* **152**, 715 (1988) & references therein.
- [3] See Y. Liang, W.-M. Mu, W. E. Packard, & J. D. Dow, *Bull. Am. Phys. Soc.* **35**, 227 (1990). L. J. Whitman, J. A. Stroscio, R. A. Dragoset, *Bull. Am. Phys. Soc.* **35**, 226 (1990) have independently reported images of the InSb(110) surface recently.
- [4] Pachyderm Scientific Industries technical report TR1000-01.
- [5] S. Y. Tong, A. R. Lubinsky, B. J. Mrstik, & M. A. Van Move, *Phys. Rev. B* **17**, 3303 (1978); D. J. Chadi, *Phys. Rev. B* **18**, 1800 (1978); **19**, 2074 (1979); D. V. Froelich, M. E. Lapeyre, J. D. Dow, & R. E. Allen, *Superlatt. Microstruct.* **1**, 87-89 (1985); R. V. Kasowski, M.-M. Tsai, & J. D. Dow, *J. Vac. Sci. Technol. B* **5**, 953-5 (1987).
- [6] W. E. Packard, N. Dai, J. D. Dow, R. C. Jaklevic, W. J. Kaiser, & S. L. Tang, *J. Vac. Sci. Technol. A* **8**, 3512 (1990).

tip
= a
ale
be
the
are
ory

S.
his
ave
of

A Dislocation-like Antiphase Boundary on a Si(111)-(7x7) Surface

Yi Wei, M.-H. Tsai, John D. Dow and I.S.T. Tsong

**Department of Physics and Astronomy
Arizona State University, Tempe, AZ 85287**

Using scanning tunneling microscopy (STM), we have observed an antiphase boundary that resembles a perfect dislocation on a Si(111)-(7x7) surface. The extra row of adatoms forming the boundary lies on the unfaulted half of the 7x7 unit cell, in agreement with total energy calculations using the first-principles self-consistent pseudofunction method. The filled-state STM image shows a missing interior adatom on the unfaulted half, in agreement with calculations of the partial density of states of an adatom surrounded by three rest-atoms.

PACS numbers: 68.35.Bs; 61.16Di; 61.70.Jc.

In recent years, scanning tunneling microscopy (STM) has been applied extensively to the study of surface defects. Specifically, atom-resolved images of dislocations have been obtained on surfaces of PbS(001)¹, Au(111)², GaAs(110)³, and PtNi(111)⁴. On the well-studied Si(111)-(7x7) surface, however, no dislocations have ever been found, although domain boundaries are frequently observed^{5,6}. These boundaries generally separate two adjacent 7x7 domains on the same terrace, with a phase slip across the boundary. The slippage is usually taken up by missing adatoms, and the boundary, more often than not, follows a wavy path. We present here the first STM images of an antiphase boundary that resembles a perfect dislocation on a Si(111)-(7x7) surface. We will also compare the filled-state image of this boundary with first principles calculations of the electronic structure in the vicinity of the boundary.

The sample used in the experiment was a n-type Si(111) wafer with a resistivity of 0.015 Ω cm. The surface was cleaned the conventional way by flashing it to 1200°C for several seconds. The base pressure of the ultrahigh vacuum chamber was $\leq 1 \times 10^{-10}$ torr and rose to 2×10^{-9} torr during flashing. After cooling to room temperature, STM images showed the familiar 7x7 reconstruction. With the sample bias at 2V, i.e. sampling unoccupied states, we observe an extra row of adatoms bisecting the two halves of a 7x7 unit cell as indicated by arrows in Fig. 1(a). The filled-state image of the same area is shown in Fig. 1(b), and we observe that one of the middle adatoms is missing on the unfaulted half of the 7x7 unit cell. The extra row of adatoms spans the entire width, $\sim 350\text{\AA}$, of a 7x7 terrace, running from an upstep edge as shown in Fig. 2(a), to a downstep edge in Fig. 2(b).

Because of its uninterrupted straight-line nature, this row of adatoms resembles a perfect dislocation emerging from the bulk to the surface. On closer inspection, however, it becomes clear that the formation of this defect does not require an extra plane of atoms in the bulk as a dislocation would. Fig. 3 depicts a plan view of the unit

cell containing the defect and also a side view across a section labelled AB. From the plan view, we see that the unfaulted half of the 7×7 unit cell undergoes a phase shift by half the distance between two adatoms, or 3.84 \AA , across the line defect. However, the extra row defect itself forms the unfaulted half of a 7×7 unit cell enclosed by dashed lines in the plan view of Fig. 3. Moreover, the entire unfaulted half (including the extra row) almost forms half of a 9×9 unit cell (minus a corner adatom). From the side view of Fig. 3, we see that the existence of an extra row of adatoms on the surface does not disturb the arrangement of bulk atoms. So this particular line defect can be considered simply as an antiphase boundary on the 7×7 surface.

The two most interesting features of our STM observations of the antiphase boundary are: (a) the extra row of adatoms forms an extension of the unfaulted half of the 7×7 , i.e. a quasi- 9×9 half unit-cell; and (b) the middle adatom of the unfaulted 7×7 , or the interior adatom of the unfaulted 9×9 , is missing in the filled-state image. In order to provide an explanation for our observations, we perform total energy, or zero-temperature free energy, calculations using the first-principles self-consistent pseudofunction method⁷.

In the model for the antiphase boundary in Fig. 3, the only adatom surrounded by three first-layer rest-atoms (located at the apexes of the dotted triangle) is the interior adatom on the quasi- 9×9 unfaulted half. All other adatoms in Fig. 3, whether on faulted or unfaulted half, have either one or two nearby rest-atoms. These rest-atoms are not directly bonded to any adatom. In view of the demanding task to perform calculations on the 7×7 surface as demonstrated recently^{8,9}, we simulate the antiphase boundary (or more precisely, the quasi- 9×9 half unit-cell) by three-fold rotationally symmetric two-dimensional unit cells with the adatom at the origin as shown in Fig. 4. In this structure, each adatom is surrounded by three rest-atoms as outlined by dotted lines in Fig. 4(a). Each unit cell contains one Si adatom and four Si atoms in each layer of a six-layer isolated slab model. Four hydrogen atoms are

attached to the bottom layer to saturate the dangling bonds. The adatoms form a 2x2 hexagonal geometry. The difference between unfaulted and faulted surfaces lies in the positions of the first layer Si atoms as shown in Figs. 4(a) and 4(b) respectively. The adatom is located at the T_4 site, which is directly above a second-layer atom. The height of the adatom above the second-layer atom is taken to be equal to the bulk Si bond length, i.e. 2.35Å. The heights of the adatoms on both unfaulted and faulted halves are taken to be the same. These are reasonable approximations because a change in the Si-Si bond length by 0.05Å only changes the bond energy by about 0.03 eV¹⁰.

In the total-energy calculations, we use three two-dimensional special k-points of Cunningham¹¹ for a hexagonal lattice to approximate the integration over the first Brillouin zone. Our calculations show that the unfaulted surface of Fig. 4(a) is more stable than the faulted surface of Fig. 4(b) by 0.33 eV per atom. The difference in energy accounts for the occurrence of the antiphase boundary on the unfaulted half, extending the 7x7 to a quasi-9x9 geometry on that half.

We have also calculated the partial density of states of the adatoms for the unfaulted surface shown in Fig. 4(a). The missing interior adatom in our filled-state image of Fig. 1(b) is similar to that reported earlier by Becker et al.¹² for a filled-state image of a Si(111)-(9x9) reconstruction in which the interior adatom was considerably darker than the corner and middle adatoms. Becker et al.¹² speculated that because three rest-atoms surrounded the interior adatom, more charges were transferred from this adatom to the rest-atoms than either the corner or middle adatoms which had fewer nearby rest-atoms. This increased charge-transfer rendered the interior adatom darker than the rest in the filled-state image.

Our calculations on the surface shown in Fig. 4(a), based on sampling energy levels of six special k-points of Cunningham¹¹, are plotted in Fig. 5. The energies are plotted relative to the calculated Fermi level of this system, which is 5.03 eV below the

vacuum level. The partial-density-of-states curve shows four peaks located at -2.7 eV, -1.2 eV, -0.2 eV and 2.0 eV. The $(dI/dV)/(IV)$ -versus-energy curve for corner adatoms measured by Wolkow and Avouris¹³ is also reproduced in Fig. 5 for comparison. The energy peaks of the $(dI/dV)/(IV)$ curve occur at -1.9 eV, -0.4 eV, 0.5 eV and 1.6 eV. Our calculated peaks differ from the measured peaks by -0.8 eV, -0.8 eV, -0.7 eV and 0.4 eV respectively. The shift of density of states towards lower energies in the filled band corresponds to the addition of a positive potential to the adatom. This fits the description of the adatom having more electronic charges transferred to the three rest-atoms such that it becomes more electropositive. The charge-transfer contributes to the dark interior adatom in the filled-state STM image in Fig. 1(b). The empty-state image in Fig. 1(a), on the other hand, shows all equally bright adatoms despite the fact that our calculations show an upward shift in energies by 0.4 eV in the conduction band. This is probably due to the more delocalized or diffused nature of the empty states further away from the Fermi level and the sampling of these states is not affected by small shifts in the partial density.

In conclusion, we have observed an antiphase boundary that resembles a perfect dislocation on the Si(111)-(7x7) surface. By performing calculations on the total energies and partial density of states using the pseudofunction method, we have explained the preferred location of the antiphase boundary on the unfaulted half of the 7x7 and the missing interior adatom on the resulting quasi-9x9 structure in the filled-state STM image.

This work was supported by the U.S. Army Research Office contracts DAAL 03-92-G-0038 and DAAL 03-91-G-0054.

REFERENCES

1. N.J. Zheng, I.H. Wilson, U. Knipping, D.M. Burt, D.H. Kinsley and I.S.T. Tsong, Phys. Rev. B 38, 12780 (1988).
2. Ch. Wöll, S. Chiang, R.J. Wilson and P.H. Lippel, Phys. Rev. B 39, 7988 (1989).
3. G. Cox, D. Szyuka, U. Poppe, K.H. Graf, K. Urban, C. Kisielowski-Kemmerich, J. Krüger and H. Alexander, Phys. Rev. Lett. 64, 2402 (1990).
4. M. Schmid, A. Biedermann, H. Stadler and P. Varga, Phys. Rev. Lett. 69, 925 (1992).
5. Th. Berghaus, A. Brodde, H. Neddermeyer and St. Tosch, Surf. Sci. 193, 235 (1988).
6. H. Tanaka, M. Udagawa, M. Itoh, T. Uchiyama, Y. Watanabe, T. Yokotsuka and I. Sumita, Ultramicroscopy 42-44, 864 (1992).
7. R.V. Kasowski, M.-H. Tsai, T.N. Rhodin and D.D. Chambliss, Phys. Rev. B 34, 2656 (1986).
8. I. Stich, M.C. Payne, R.D. King-Smith, J.-S. Lin and L.J. Clarke, Phys. Rev. Lett. 68, 1351 (1992).
9. K.D. Brommer, M. Needles, B.E. Larson and J.D. Joannopoulos, Phys. Rev. Lett. 68, 1355 (1992).
10. M.-H. Tsai, J.D. Dow and R.V. Kasowski, Phys. Rev. B 38, 2176 (1988).
11. S.L. Cunningham, Phys. Rev. B 10, 4988 (1974).
12. R.S. Becker, B.S. Swartzentruber, J.S. Vickers and T. Klitsner, Phys. Rev. B 39, 1633 (1989).
13. R. Wolkow and Ph. Avouris, Phys. Rev. Lett. 60, 1049 (1988).

FIGURE CAPTIONS

Fig. 1 (a) Empty-state and (b) filled-state STM images of a dislocation-like antiphase boundary, indicated by arrows, on a Si(111)-(7x7) surface. Scan area = $150\text{\AA} \times 150\text{\AA}$. Tunnel current = 1 nA. Sample bias = 2V for (a) and -1V for (b). The 7x7 unit cell is outlined.

Fig. 2 STM images of the antiphase boundary (indicated by arrow) running across the full width, $\sim 350\text{\AA}$, of a 7x7 terrace from (a) the upstep edge to (b) the downstep edge. Scan area = $200\text{\AA} \times 200\text{\AA}$. Tunnel current = 1 nA. Sample bias = 2V.

Fig. 3 A structural model for the antiphase boundary showing a plan view and a side view across a section AB. The faulted and unfaulted halves are labeled F and U respectively. The dashed lines enclose the antiphase boundary forming an almost perfect 7x7 geometry. The unfaulted half has a quasi-9x9 structure (minus a corner adatom) with an interior adatom surrounded by three rest-atoms at the apexes of the dotted triangle. This interior adatom appears missing in the filled-state image in Fig. 1(b).

Fig. 4 Plan-view models of the unfaulted surface (a) and faulted surface (b) used in our calculations. ● Si adatom; O first-layer Si; o second-layer and third-layer Si; x fourth-layer Si. In this model, each adatom is surrounded by three rest-atoms located at the apexes of the dotted triangle in (a). The Si adatoms form a 2x2 unit cell outlined in both (a) and (b).

Fig. 5 (a) The partial density of adatom states calculated for the surface shown in Fig. 4(a). (b) The $(dI/dV)/(I/V)$ curve of Wolkow and Avouris¹³ for a corner adatom on a 7x7 surface. The energy peaks in each curve are labeled 1 through 4.

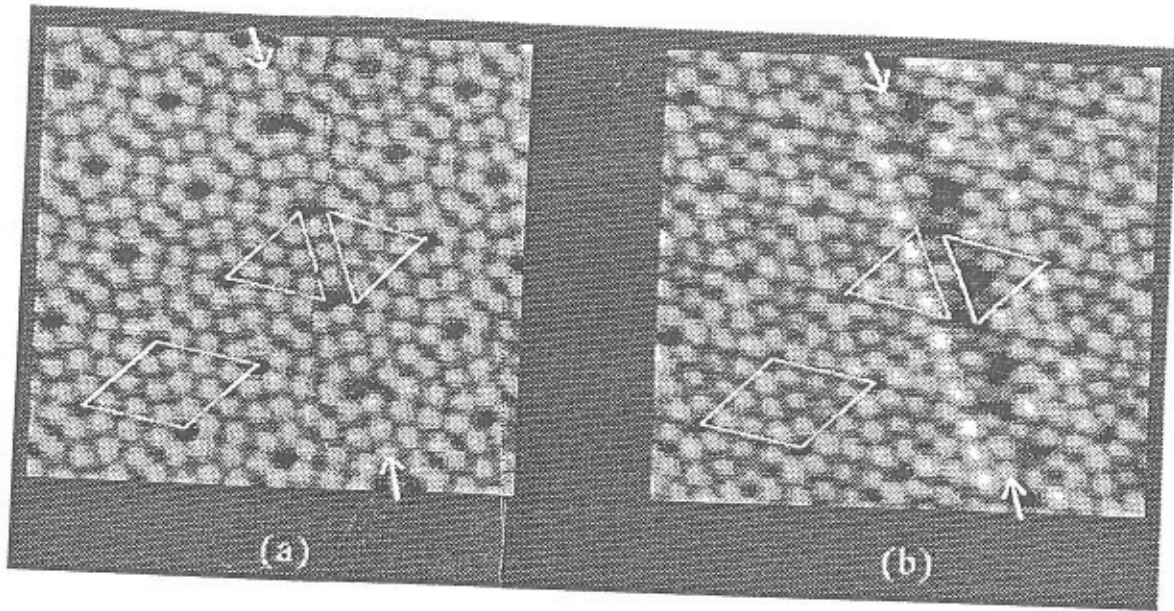


Fig. 1

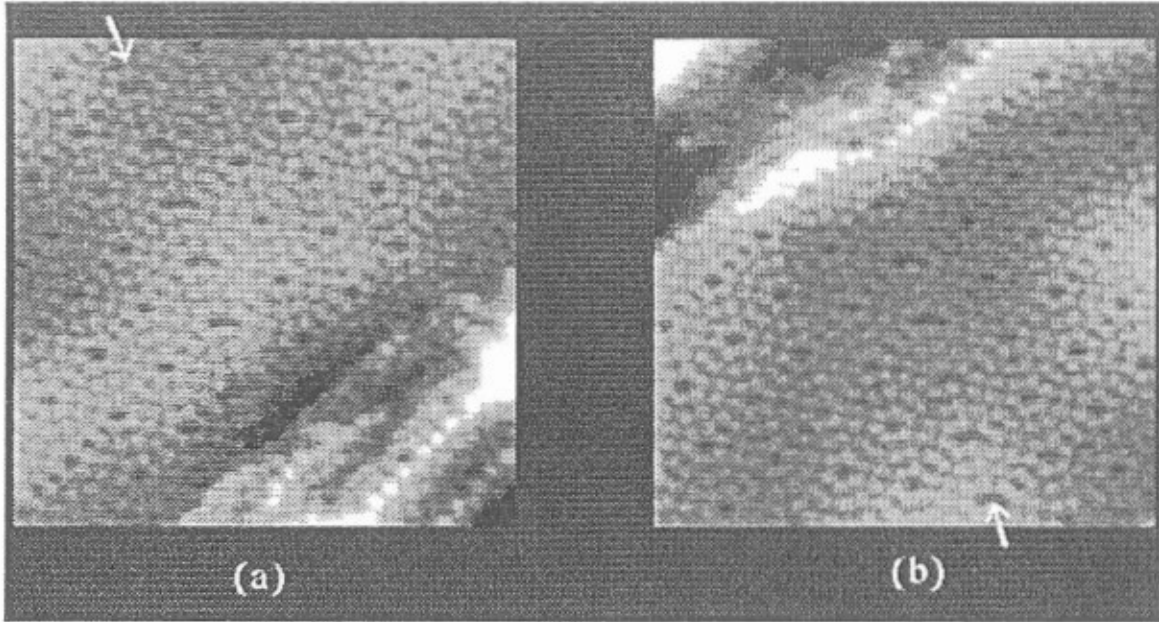


Fig. 2

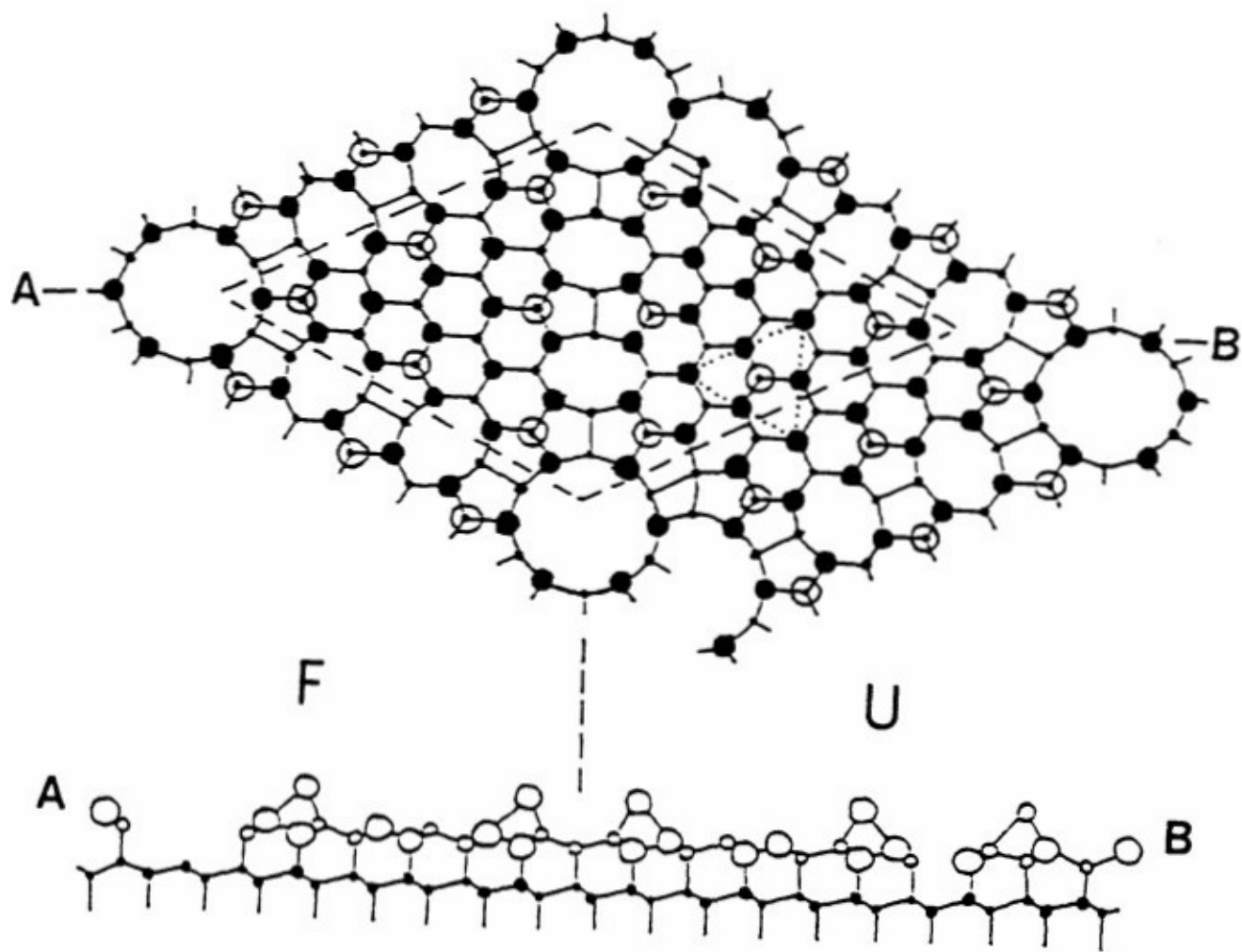


Fig. 3

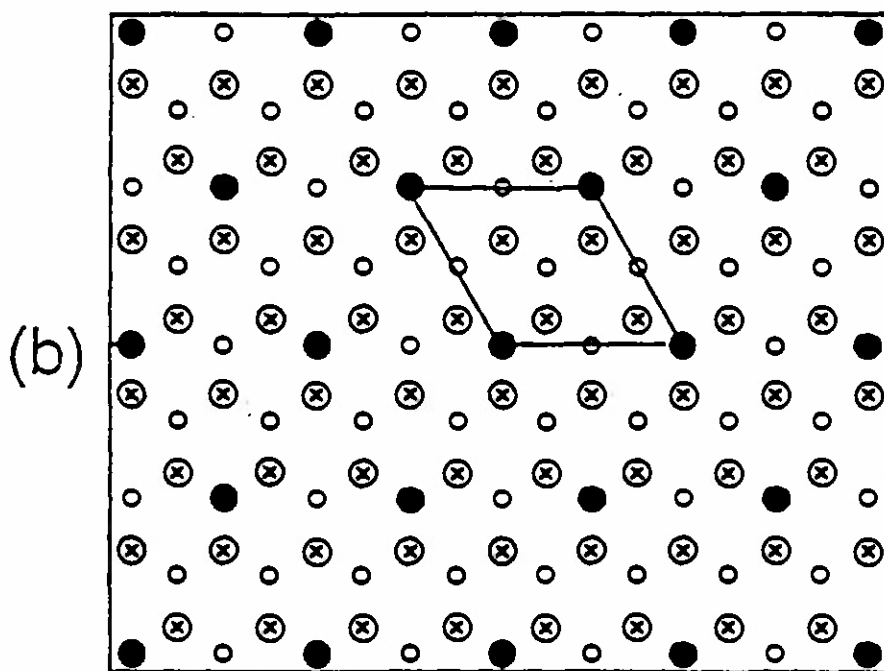
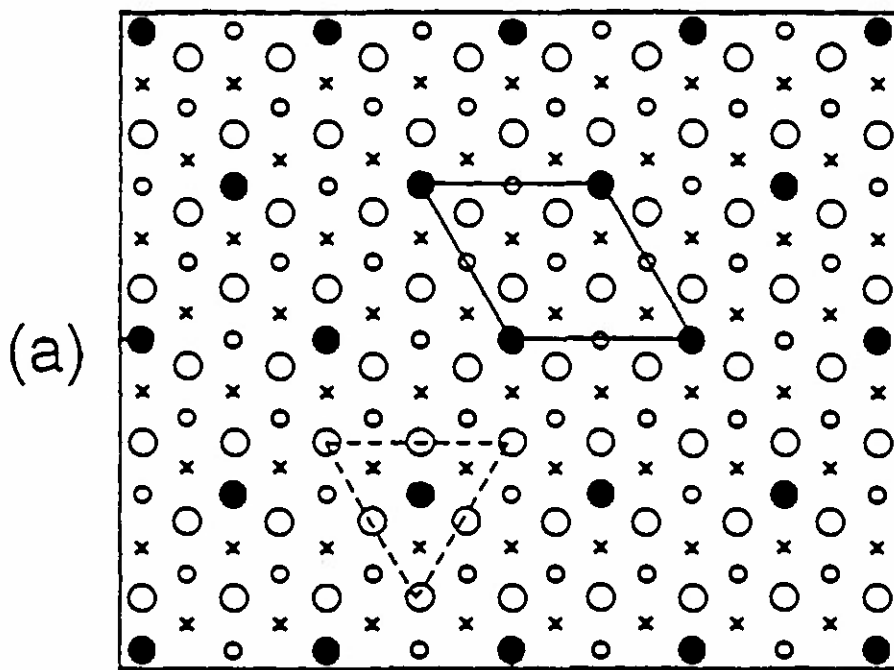


Fig. 4

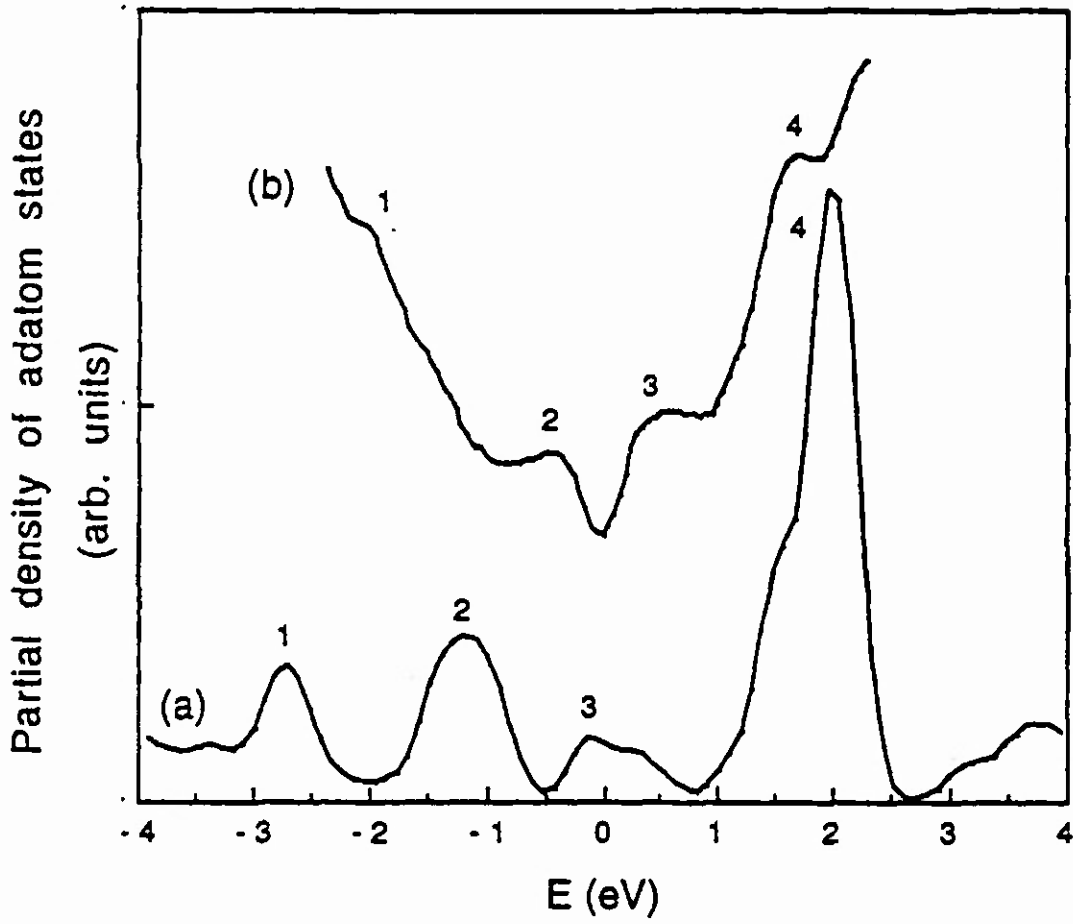


Fig. 5

Ethereal "interstitials" on the (110) surface of InSb

Yong Liang*

Department of Physics, University of Notre Dame, Notre Dame, Indiana 46556
and

Department of Physics and Astronomy, Arizona State University
Tempe, Arizona 85287-1504 U.S.A.

and

Min-Hsiung Tsai, William E. Packard, and John D. Dow
Department of Physics and Astronomy, Arizona State University
Tempe, Arizona 85287-1504 U.S.A.

and

Howard A. Blackstead
Department of Physics, University of Notre Dame
Notre Dame, Indiana 46556 U.S.A.

(Received 4 December 1992 by J. Tauc)

Scanning tunneling microscopy (STM) images of the (110) surface of InSb reveal apparent surface interstitial Sb atoms when the sample bias voltage is small and negative, corresponding to tunneling of electrons from the top of the valence band of InSb. These surface "interstitials" disappear at other bias voltages. The observations of these "ethereal interstitials" are explained in terms of *below-surface, second-layer Sb atoms*, that appear to lie above the surface due to the re-hybridized character of the surface Sb wavefunctions near the top of the valence band.

1. Introduction

In this Communication, we report scanning tunneling microscopy (STM) measurements of the InSb (110) surface under conditions of small negative sample bias (tunneling of electrons from near the top of the InSb valence band to the STM tip). We find an apparent face-centered rectangular surface crystal structure (Fig. 1), in conflict with the expectation of a simple-rectangular surface crystal structure of Sb atoms. In fact the atom at the face-center is brighter than the other four atoms of the unit cell at some bias voltages, and appears to be an above-surface interstitial atom — with there being one “interstitial” per surface unit cell. Under negative bias, only Sb atoms are expected to be imaged; but these “interstitials” lie neither at the positions of surface In atoms nor of surface Sb atoms, based on the expected “rigid rotation” geometry of the (110) surface relaxation of InSb [1-7].

By increasing the magnitude of the bias voltage, we are able to reduce the strength of the “interstitial” image, until all of the “interstitials” disappear simultaneously in all unit cells. Clearly these ethereal images of “interstitial”-like features, which disappear simultaneously in every unit cell as the magnitude of the bias voltage is varied, are unlikely to be images of actual interstitial atoms on the surface.

In the remainder of this paper we describe how the data are taken, and present theoretical arguments to the effect that the “ethereal interstitials” are in fact second-layer Sb atoms that become rather bright in comparison with the surface Sb atoms (and hence appear to lie above the surface) because they are associated with states near the top of the valence band of InSb.

2. Experiment

For these studies, we used a Pachyderm-4 cleavage scanning tunneling microscope, which has been described in detail elsewhere [8]. The InSb samples were nominally undoped single-crystal bars manufactured by Sumitomo. Before each STM experiment, each sample

was freshly cleaved in UHV ($\approx 10^{-10}$ torr), producing a mirror-like flat surface. The microscope tips were made of W which had been electrochemically etched in an NaOH solution.

For sample biases of a few tenths of a Volt, the expected rectangular surface crystal structure was observed [8], consisting of Sb (In) atoms for negative (positive) sample bias. When the magnitude of the negative bias was reduced to ≈ 0.05 V, the ethereal interstitials appeared at the center of each surface unit cell (Fig. 1). The intensity of this feature relative to the intensity of the Sb corner-atom intensity varied reproducibly from zero to greater than unity as the magnitude of the bias voltage was reduced from a few tenths of a Volt (or more) to 0.05 V. The smallest and best bias voltage magnitude was 0.05 V; below this, no features could be seen.

3. Theory

The ethereal interstitial features lie directly above the sites of second-layer Sb atoms (Fig. 2), and so we investigated the possibility that somehow those second-layer atoms could produce an image that appeared to have an above-surface interstitial for biases of order -0.05 V, but would have that feature disappear for a more-negative bias of -0.3 V.

To do this, we calculated the expected images for biases of -1.5 V and -0.05 V, producing the results of Fig. 3. Note that the "ethereal interstitial" feature does appear prominently in Fig. 3b (-0.05 V), but not in Fig. 3a (-1.5 V), and therefore is explained by the theory. In fact, Fig. 4 shows the intensity ratio, I_2 of the "ethereal interstitial" peak to I_1 for the 1×1 peaks (the corners of the surface unit cell), showing that the theory and the data exhibit the same general trends as the bias is varied.

The theoretical calculations rely on Bardeen's approximation for the tunneling current [9]:

$$I(V) = (2\pi e/\hbar) \sum_{\mu,\nu} f(E_\mu)[1-f(E_\nu - eV)] \times |M_{\mu,\nu}|^2 \delta(E_\mu - E_\nu), \quad (1)$$

where $f(E)$ is the Fermi factor, $M_{\mu,\nu}$ is the transfer ma-

trix element between the sample state ν and the tip state μ , and V is the bias voltage. Tersoff and Hamann [10] have obtained an approximate expression for the tunneling current, valid for small V :

$$I(V) \propto V \sum_{\nu} |\psi_{\nu}(\mathbf{R}_{\text{tip}})|^2 \delta(E_{\nu} - E_{\text{F}}), \quad (2)$$

where $\psi_{\nu}(\mathbf{R}_{\text{tip}})$ is the electronic wavefunction of the sample state ν at the tip position \mathbf{R}_{tip} , and E_{F} is the Fermi energy. The summation on the right hand side of Eq. (2) is basically an energy-selected charge density (for filled states) or a virtual energy-selected charge density (for empty states) at the tip position, and was obtained by Taylor expansion of Bardeen's formula to lowest order in V . As such, the Tersoff-Hamann expression allows tunneling for states at E_{F} only and does not contain the Fermi factors of Eq. (1), which allow tunneling for states with energies between E_{F} and $E_{\text{F}} - eV$. Nevertheless it is reasonable to extend Eq. (2) to higher bias voltages by replacing the δ -function with a window function that is unity within the interval $(E_{\text{F}}, E_{\text{F}} - eV)$ and zero elsewhere. We further simplify our calculation by assuming that the STM image, which is measured under constant-current conditions, is adequately simulated by the energy-selected charge density at a constant tip-height of 5 Å above the surface.

The computations were executed using the local-density approximation as implemented with the well-established pseudofunction method [11] — a method which has successfully described the electronic and optical properties of many solids [12] and solid surfaces [13]. Details of the calculational approach are available in Ref. [11].

4. Results

Because of the p-like anion-like character of the electronically filled states of zinc-blende semiconductors, STM images of (110) surfaces for negative sample bias (namely for tunneling of electrons from the valence band to the STM tip) are expected to show the anion atoms at the surface, and these exhibit a rectangular unit cell for the (110) surface. Under such bias conditions, the cation atoms are not normally visible. Thus the charac-

teristic signature of tunneling from a zinc-blende (110) surface is a rectangular unit cell of anion atoms. This signature has been observed in the STM data for the InSb (110) surface [8] and the (110) surfaces of other III-V zinc-blende semiconductors [14], for moderate to large bias magnitudes, and in the theory of Fig. 3.

The striking fact is that the theory also reproduces the unexpected "ethereal interstitial" feature for small negative biases, and that this feature is associated with a directed p-orbital centered on a sub-surface Sb atom [15-17]. In the early days of scanning tunneling microscopy it was generally believed that the STM image is a topograph, giving a picture of the surface atoms, with image intensities reflecting heights indicative of the actual surface atoms' sizes. This belief seems to be held by some workers even today. The ethereal interstitials necessarily fall outside this notion of topographic images, because they correspond to second-layer Sb atoms that are expected to be invisible due to their lack of height, and yet are observed to be brighter than first-layer atoms at small bias voltages. By dissecting our calculations, we find that the relative prominence of the "ethereal interstitials" is due to the relative amplitudes of surface and sub-surface Sb wavefunctions at near-zero bias. The tunneling conditions for small negative bias are such that only electrons from near the top of the InSb valence band (at $k=0$) participate in the tunneling. At $k=0$ the wavefunction is quasi-uniform throughout the crystal and one would expect the first-layer wavefunction to produce a brighter image, were it not for the following: (i) The surface sp^3 bonds re-hybridize as a result of surface relaxation [16] and their contribution to the tunneling in the energy range between E_F and $E_F - 0.05$ eV is reduced because they dangle into the vacuum less in this spectral region. In contrast, the more distant sub-surface bonds still point toward the surface and contribute strongly to the tunneling; and (ii) The surface atoms' wavefunctions have evanescent tails which decay exponentially away from the surface, whereas the sub-surface atoms have wavefunctions with Wigner-Seitz boundary-condition dangling tails that are not appreciably attenuated until they reach the surface. Primarily the first of these two effects causes the wavefunction amplitudes of the surface atoms to be smaller,

and is responsible for the darkening surface atom images and the appearance of the second-layer atoms as relatively brighter. But as the wavefunctions of the tunneling electrons become less $k=0$ -like on the average, namely, as the bias voltage becomes more negative, the dangling-bond states at the surface, which are spectrally concentrated at energies in the valence band, contribute more to the tunneling and eventually dominate it. Then the "ethereal interstitial" becomes (relatively) less prominent, with its relative intensity exhibiting the same trend with bias voltage as the theory (Fig. 4). Evidence supporting this viewpoint, that the surface atoms are darker in the image due mostly to their being re-hybridized at a relaxed surface, is that the ethereal interstitials are not visible in the image computed for the *unrelaxed* surface under the same bias conditions.

Frequently one expects a topographic image from an STM experiment [18], but non-topographic images with bright second-layer atoms, similar to what we have found here, do occur: Hamers *et al.* [19] have reported images with sub-surface features for the clean Si (111) 7×7 surface. Tsai *et al.* have reported β -SiC (111) surfaces in which the carbonaceous surface forms a graphitic monolayer, and the STM images are dominated by tunneling from those second-layer Si dangling bonds that are not masked by the graphitic surface layer [20].

5. Summary

We have observed InSb (110) surface structures by STM under negative bias that feature what appear to be interstitial atoms in every unit cell, and the interstitials appear to lie *above* the surface defined by the four Sb atoms in the surface unit cell. These apparent interstitials are in fact sub-surface Sb atoms that are relatively prominent in the STM images taken at small negative bias voltages, but disappear as the magnitude of the bias is increased.

Our results illustrate the fact that non-topographic images can appear — and can be very deceptive unless one carefully compares theory with data.

Acknowledgement — We are grateful to the U.S. Army Research Office (Contract DAAL03-91-G-0054), the U.S. Air Force Office of Scientific Research (Contract No. AFOSR-91-0418), and the U.S. Office of Naval Research (Contract No. N00014-92-J-1425) for their generous support. We thank Dr. L. J. Whitman, whose suggestion that the ethereal interstitial might be a tip effect, led us to check that possibility very carefully.

REFERENCES

- * Present Address: Laboratory for Research on the Structure of Matter, University of Pennsylvania, Philadelphia, Pennsylvania 19104.
- [1] S. Y. Tong, A. R. Lubinsky, B. J. Mrstik, and M. A. Van Hove, *Phys. Rev. B* **17**, 3303 (1978).
 - [2] D. J. Chadi, *Phys. Rev. B* **18**, 1800 (1978); D. J. Chadi, *Phys. Rev.* **19**, 2074 (1979).
 - [3] There is a controversy over whether the surface relaxation angle depends on ionicity or not, with Refs. [4] and [5] arguing that it does, while Ref. [6] argues that it does not. The data of Ref. [7] are compatible with Refs. [4] and [5].
 - [4] R. V. Kasowski, M.-H. Tsai, and J. D. Dow, *J. Vac. Sci. Technol.*, **B 5**, 953 (1987); M.-H. Tsai, J. D. Dow, R.-P. Wang, and R. V. Kasowski, *Phys. Rev. B* **40**, 9818 (1989); *Superlatt. Microstruct.* **6**, 431 (1989).
 - [5] J. L. A. Alves, J. Hebenstreit, and M. Scheffler, *Phys. Rev. B* **44**, 6188 (1991).
 - [6] For InSb (110), see C. B. Duke, R. J. Meyer, and P. Mark, *J. Vac. Sci. Technol.* **17**, 971 (1980); for a review of more recent work by Duke and co-workers, see W. Chen, M. Dumas, S. Ahsan, A. Kahn, C. B. Duke, and A. Paton, *J. Vac. Sci. Technol. A* **10**, 2071 (1992); A. Kahn, S. Ahsan, W. Chen, M. Dumas, C. B. Duke, and A. Paton, *Phys. Rev. Letters* **68**, 3200 (1992), and references therein. Note that while most of the earlier work relies on analyses of low-energy electron diffraction data and comes to the conclusion that all zinc-blendes have essentially the same surface relaxation angle, recent work analyzing low-energy positron diffraction data (Ref. [7]) find an InP (110) surface relaxation angle that is significantly different from that for GaAs (110). The final resolution of this controversy lies in the future.
 - [7] X. M. Chen, G. R. Brandes, K. F. Canter, C. B. Duke, D. Paton, W. K. Ford, and D. L. Lessor, *Bull. Amer. Phys. Soc.* **37**, 167 (1992).
 - [8] Y. Liang, W. E. Packard, and J. D. Dow, *J. Vac.*

- Sci. Technol. B 9, 730 (1991); Superlatt. Microstruct. 11, 461 (1992).
- [9] J. Bardeen, Phys. Rev. Letters 6, 57 (1961).
- [10] J. Tersoff and D. R. Hamann, Phys. Rev. B 31, 805 (1985).
- [11] R. V. Kasowski, M.-H. Tsai, T. N. Rhodin, and D. D. Chambliss, Phys. Rev. B 34, 2656 (1986).
- [12] See, for example, A. Franciosi, A. Wall, Y. Gao, J. H. Weaver, M.-H. Tsai, J. D. Dow, R. V. Kasowski, R. Reifenberger, and F. Pool, Phys. Rev. B40, 12009 (1989); A. Wall, A. Franciosi, Y. Gao, J. H. Weaver, M.-H. Tsai, J. D. Dow, and R. V. Kasowski, J. Vac. Sci. Technol. A7, 656 (1989); M.-H. Tsai, J. D. Dow, and R. V. Kasowski, Phys. Rev. B 38, 2176 (1988).
- [13] See, for example, M.-H. Tsai and R. V. Kasowski, Bull. Amer. Phys. Soc. 32, 865 (1987); R. V. Kasowski and M.-H. Tsai, Phys. Rev. Lett. 60, 546 (1988). T. Kendelewicz, P. Soukiassin, R. S. List, J. C. Woicik, P. Pianetta, I. Lindau, and W. E. Spicer, Phys. Rev. B37, 7115 (1988).
- [14] R. M. Feenstra, J. A. Stroscio, J. Tersoff, and A. P. Fein, Phys. Rev. Letters 58, 1192 (1987); L. J. Whitman, J. A. Stroscio, R. A. Dragoset, and R. J. Celotta, J. Vac. Sci. Technol. B 9, 770 (1991).
- [15] The Sb p_z -orbitals responsible for the second-layer Sb's STM image also contribute to Sb-like (110) surface-state resonances of the second layer, that are believed to lie below the valence band maximum of InSb by much more than 0.05 eV (about 0.3 eV [16]). We did not detect any such states in the fundamental band gap, although we would have expected to if these states had fallen into the gap. Thus the situation for InSb, both theoretically and experimentally, appears to be similar to that for GaAs [16,17], with surface-state resonance bands much wider than 0.05 eV lying entirely *below* the valence band maximum. Hence the surface-state resonances themselves may be ruled out as causing the "ethereal interstitial" images for the following reasons: (i) Their energies are very likely outside the range accessible for the bias conditions; (ii) The shape of the curve in Fig. 4 is not a bump with the surface-state band-width, as one might ex-

pect for conventional surface-state tunneling; (iii) The "ethereal interstitial" image's prominence as the bias voltage becomes small in magnitude results primarily from the *darkening* of the image of the surface layer, not from an increase in the brightness of the second layer Sb, and so the physics that *changes* and makes the second-layer states visible actually occurs on the surface layer.

- [16] R. P. Beres, R. E. Allen, and J. D. Dow, Phys. Rev. B 26, 5702 (1982); Solid State Commun. 45, 13 (1983). See also C. Mailhot, C. B. Duke, and D. J. Chadi, Phys. Rev. B 31, 2213 (1985); Phys. Rev. B 30, 1109 (1984).
- [17] G. P. Williams, R. J. Smith, and G. J. Lapeyre, J. Vac. Sci. Technol. 15, 1249 (1978); A. Huijser, J. van Laar, and T. L. van Rooy, Phys. Letters 65a, 337 (1978).
- [18] W.-M. Hu and J. D. Dow, J. Vac. Sci. Technol. B 7, 907 (1989).
- [19] R. J. Hamers, R. M. Tromp, and J. E. Demuth, Phys. Rev. Letters 56, 1972 (1986).
- [20] M.-H. Tsai, C. S. Chang, J. D. Dow, and I. S. T. Tsong, Phys. Rev. B 45, 1327 (1992).

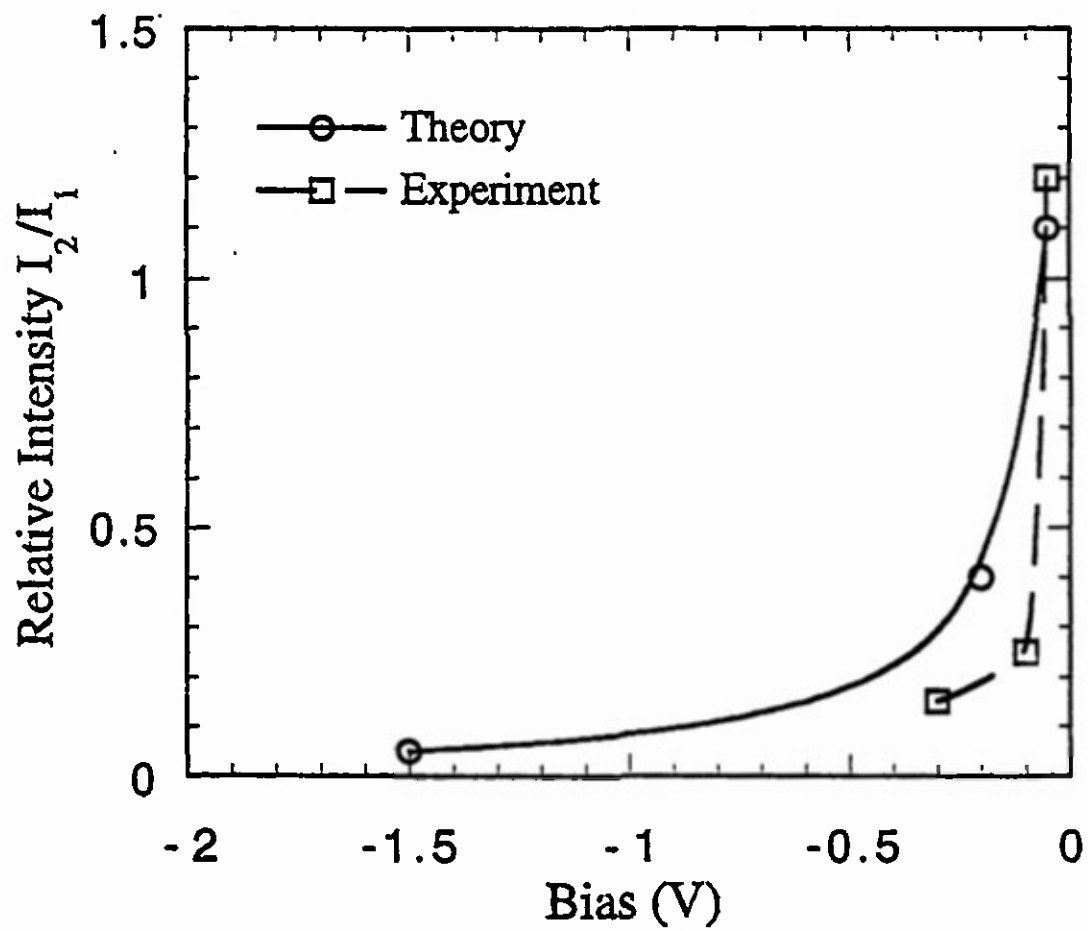
FIGURE CAPTIONS

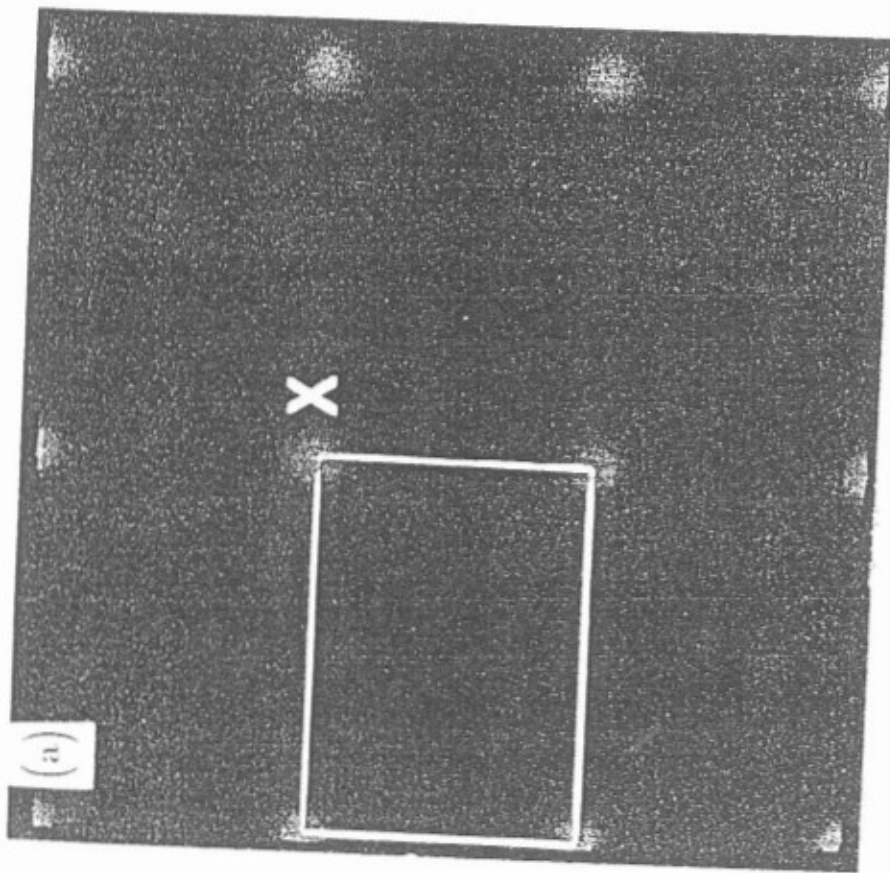
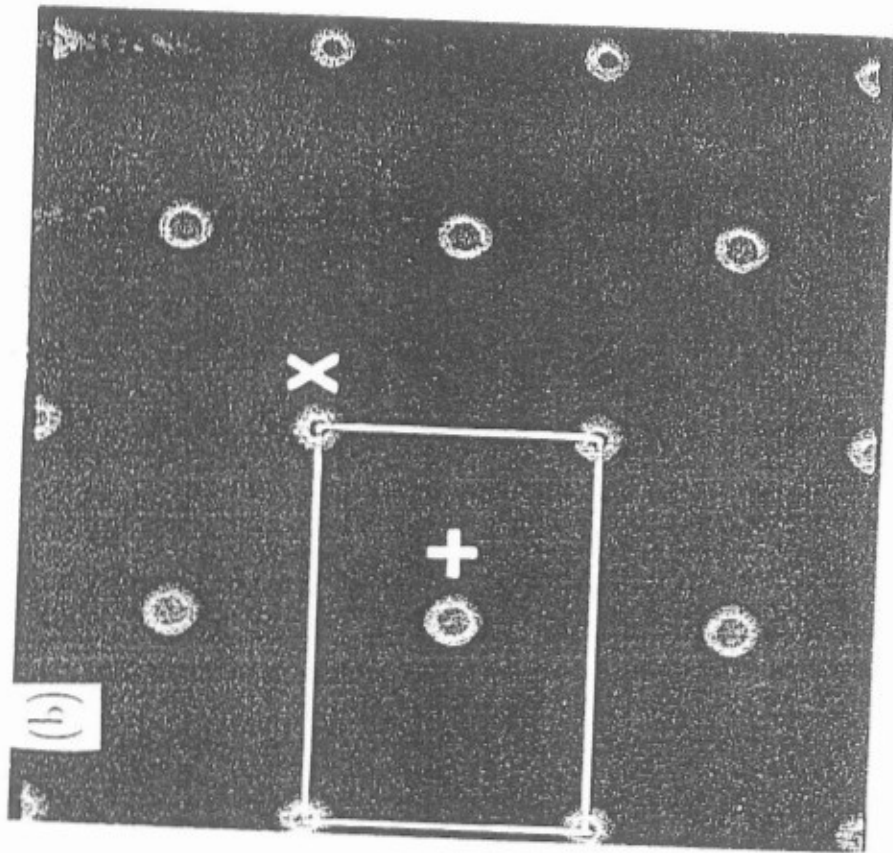
Fig. 1. STM image of the InSb (110) surface taken at a sample bias of -0.05 V. Note the prominent "interstitial" at the face-center of the unit cell, labeled by + and surrounded by less bright Sb atoms on the corners of a rectangular unit cell.

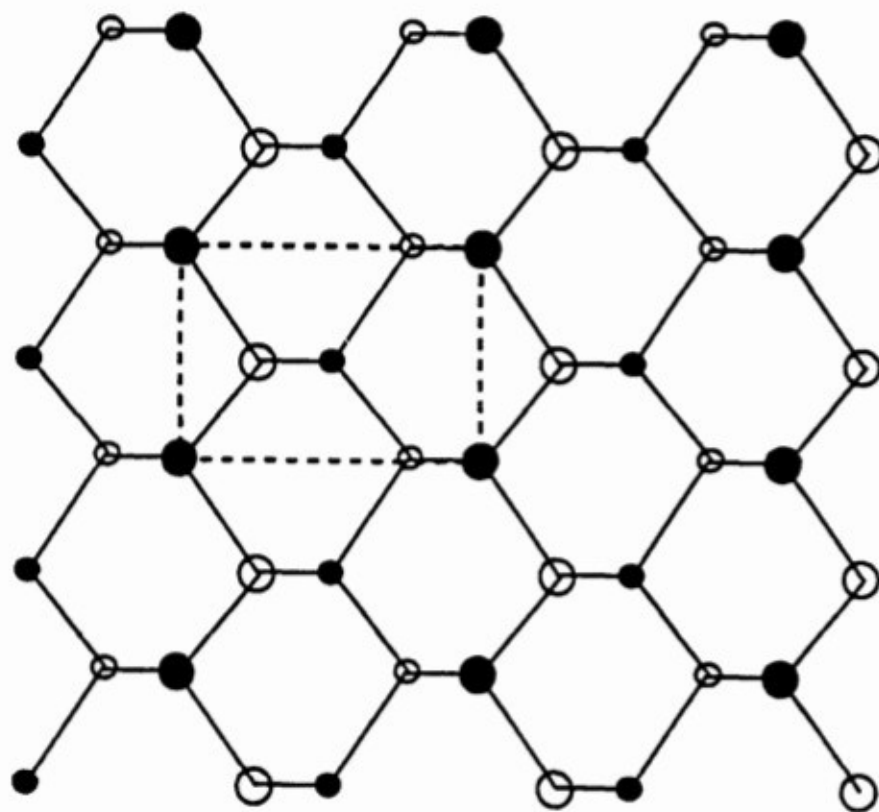
Fig. 2. Top view, looking down, of the (110) InSb surface, with the Sb atoms (solid circles) and the In atoms (open circles). The surface unit cell is dashed. The second-layer Sb is denoted by a small solid circle, and is directly below the apparent position of the "ethereal interstitial."

Fig. 3. Calculated STM image of the InSb (110) surface, as discussed in the text. (a) Image for a sample bias of -1.5 V, showing the expected 1×1 rectangular unit cell, with an Sb atom slightly to the left of the "x". (b) Image for a bias of -0.05 V, showing the "ethereal interstitial" at the face-centered site with the "interstitial" just to the left of the "+" and a corner atom of the 1×1 cell to the left of the "x".

Fig. 4. Theoretical (circles) and experimental (squares) intensity ratios I_2/I_1 versus bias voltage (in V) for the InSb (110) surface. I_2 is the intensity of the "ethereal interstitial" peak, and I_1 is the intensity of the corner Sb atoms of the 1×1 surface unit cell.







$[1\bar{1}0]$



$[001]$

Sb In

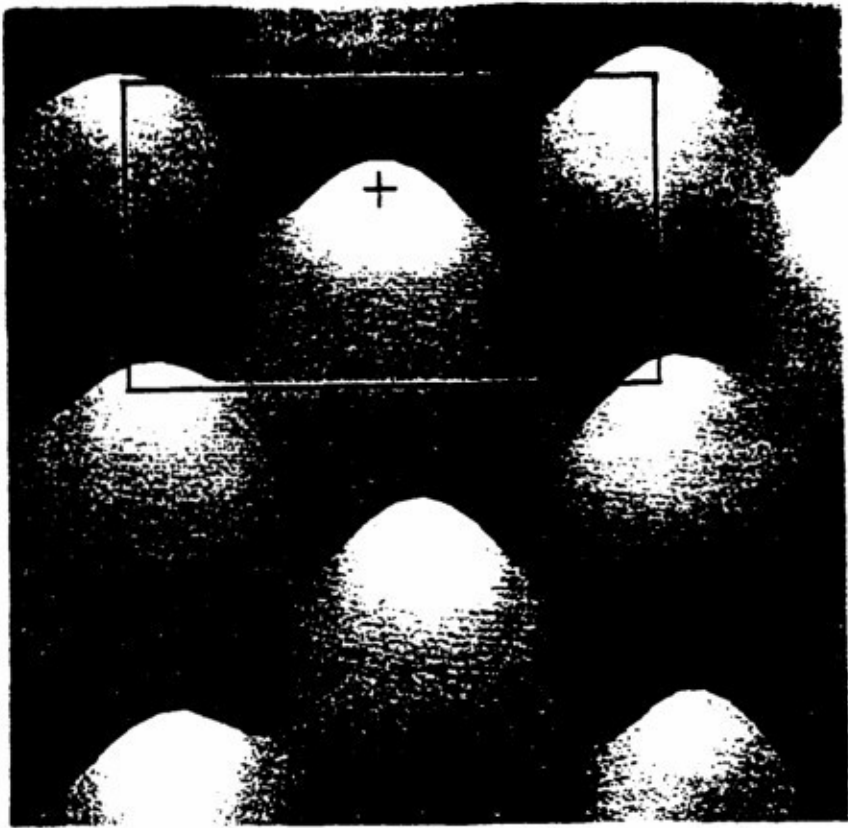


First layer



Second layer

Fig. 2



STEPS ON THE (110) SURFACE OF InP

YONG LIANG,*† WILLIAM E. PACKARD,* AND JOHN D. DOW*

*Department of Physics and Astronomy, Arizona State University, Tempe, Arizona 85287-1504, U.S.A.

†Laboratory for Research on the Structure of Matter, University of Pennsylvania, Philadelphia, Pennsylvania 19104, U.S.A.†

ABSTRACT

Three types of steps are observed on the cleaved InP(110) surface, using atomic-resolution ultra-high vacuum (UHV) scanning tunneling microscopy (STM). The step edges are oriented along the (110), (111), and (112) directions. Atomic models of monatomic-height (111) and (112) steps indicate that the edges of each of these unrelaxed steps should have pairs of dangling bonds. We propose that the bonds dimerize, causing the edges to relax and form periodic structures along the edge.

I. INTRODUCTION

In this paper we present scanning tunneling microscopy (STM) images of the InP(110) surface cleaved in ultra-high vacuum, and find atomic-resolution images of steps on this surface. Ebert *et al.* [1] have examined the InP(110) surface with STM, but the present paper is, we believe, one of the first STM efforts [2] to study such steps, which are important as nucleation sites for layered InP(110) growth, very likely determine essential physics of contact metallization, doubtless play a role in Schottky barrier formation, and getter defects. Here we present images of the flat (110) surface and of steps on the surface. We also propose a Dimerization Model of atomic relaxation at (112) step edges on the (110) surface.

II. EXPERIMENT

The images were obtained with a Pachyderm-4 ultra-high vacuum (UHV) scanning tunneling microscope equipped with a demountable sample holder containing six samples at one time. Each sample was cleaved in UHV (10^{-11} torr range) before being imaged with the tungsten tip of the STM. The microscope, cleavage method, and tip preparation are described in detail elsewhere [3].

III. RESULTS AND DISCUSSION

We imaged the (110) surface of InP with atomic resolution. An example of a flat (110) surface imaged by tunneling into the empty conduction band states is shown in Fig. 1. Similar images for the InSb(110) surface may be found in Ref. [3]. In all cases the expected 1×1 rectangular lattice was observed, and only one atomic species was imaged at a time, depending on the polarity of the sample bias: indium atoms for positive bias, and phosphorus atoms for negative bias.

In addition to flat terraces, steps on these surfaces were also observed. For InP(110), steps were found with edges running in the (110), (111), and (112) directions. An example showing all three step types on InP(110) is shown in Fig. 2, where a single triangular-shaped terrace was formed by intersecting (110), (111), and (112) steps. This intersection of steps on the (110) surface of InP was unanticipated. These steps are the result of the cleavage process and do not represent an equilibrium step configuration, as for some heat-treated samples. On Si and Ge (001)- 2×1 and (111)- 7×7 surfaces, the steps are normally created not by cleavage but by high temperature processing, namely under quasi-equilibrium conditions. Our steps on the InP(110) surface

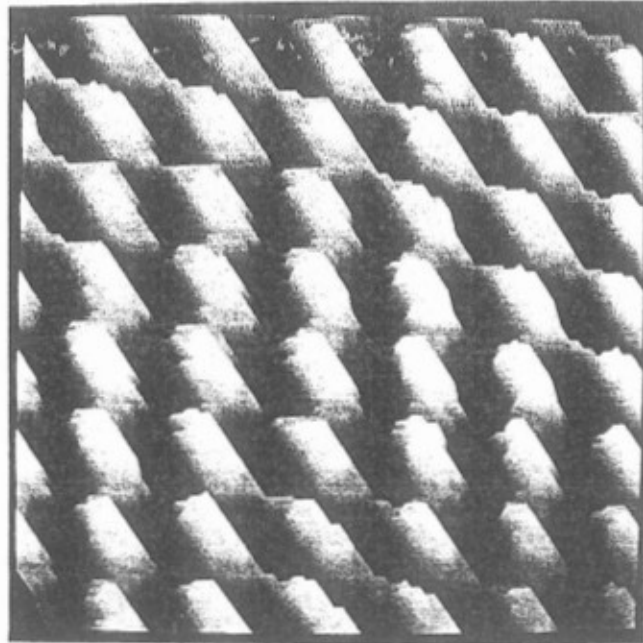


Fig. 1. STM image showing empty states on the flat, cleaved InP(110) surface: A $35 \text{ \AA} \times 35 \text{ \AA}$ image taken under +2.0 V sample bias with a tunneling current of 100 pA.

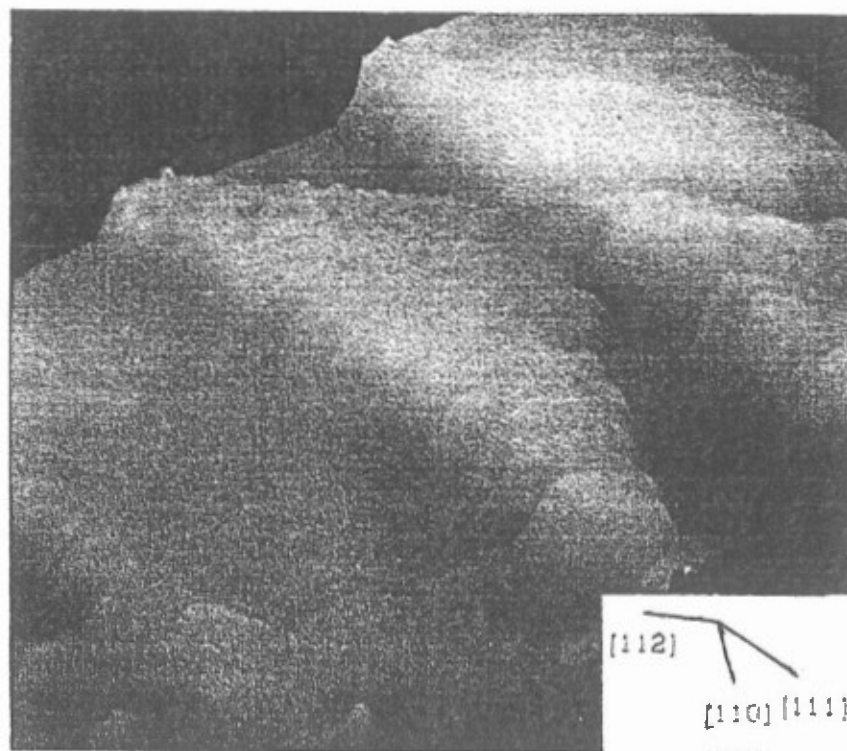


Fig. 2. Triangular terrace on the InP(110) surface, observed by STM at a voltage of +2.0 V and a current of 100 pA. A triangular structure formed by intersecting (110), (111), and (112) steps on the InP(110) surface is pictured. The region shown is $450 \text{ \AA} \times 450 \text{ \AA}$.

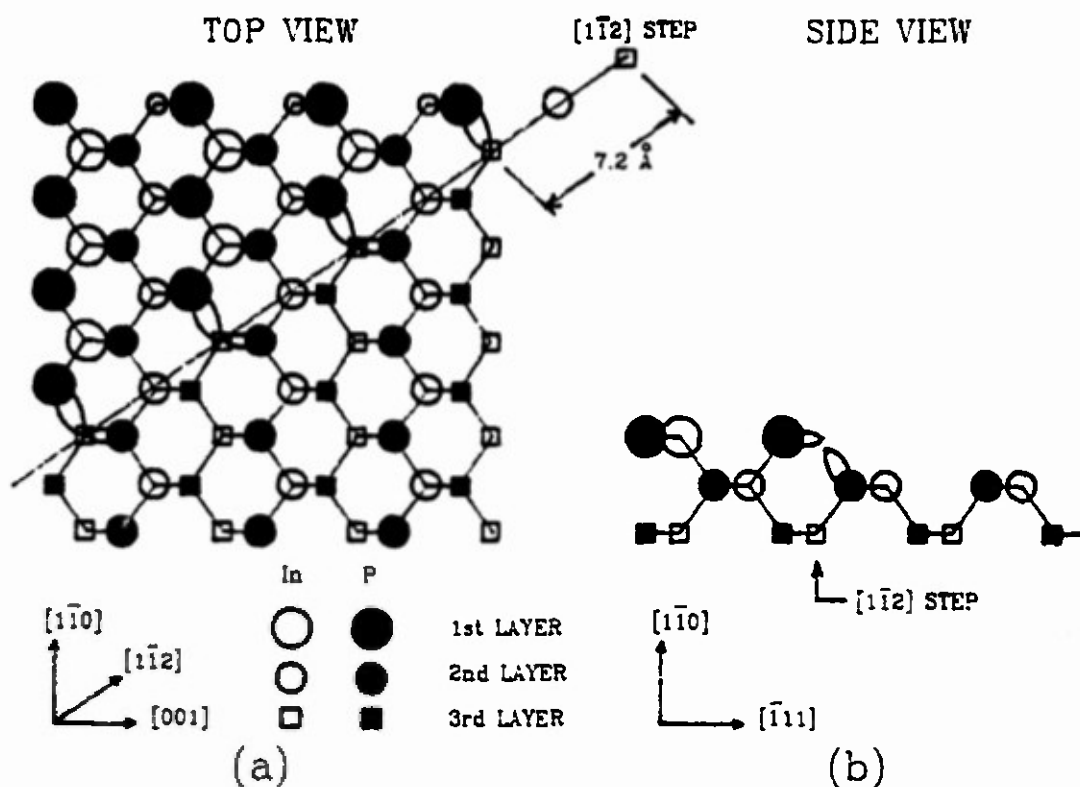


Fig. 3. Dimerization Model for a (112)-type step edge, the $[1\bar{1}2]$ step edge, *before any relaxation*. (a) Top view and (b) side view of the $[1\bar{1}2]$ step showing dangling bonds ("rabbit ears") *before* dimerization.

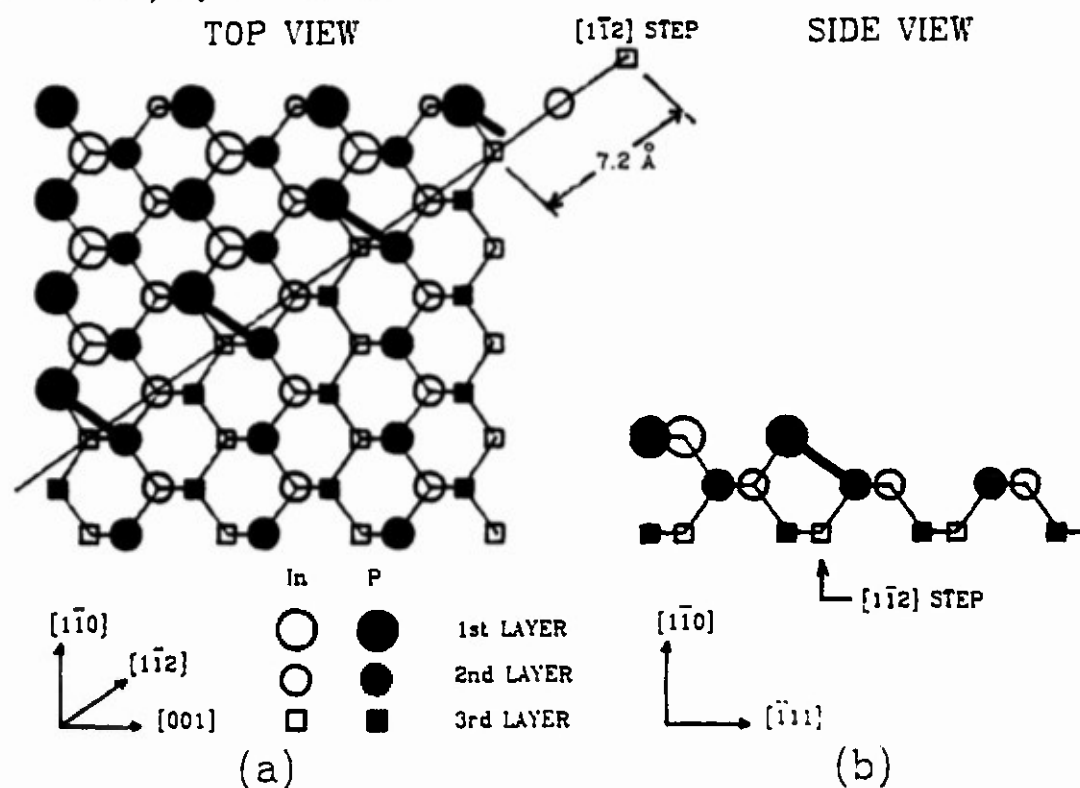


Fig. 4. Dimerization Model for a (112)-type step edge, the $[1\bar{1}2]$ step edge, *after dimerization*. For simplicity of presentation, the 29° rigid rotation [6] of the P anions up out of the surface has been omitted. (a) Top view and (b) side view of the $[1\bar{1}2]$ step showing dangling bonds *after* dimerization.

are not created in quasi-equilibrium, but by cleavage (a rather non-equilibrium event). If, on the one hand, step-intersections on the InP(110) surface were to occur at equilibrium, then those steps would have effective attractive interactions. On the other hand, if the step intersections are a result of cleaving, then the physics of their intersections should produce insights into the processes by which the cleaving energy is dispersed.

Simple geometric models of one-atom-high steps can be constructed from the zincblende (110) surface structure. Fig. 3 shows a (112)-type step, assumed to be one-atom in height, both top and side views. Note that there are two dangling bonds periodically repeated at the step-edge, one parallel to the surface and another directed at an angle of 55° with respect to the surface plane.

We propose that these bonds will dimerize and the step-edge will relax, forming the surface structure of Fig. 4. One implication of this Dimer Model of the (112)-type monatomic step is that the relaxed step-edge should be scalloped, showing a periodic structure of about 7.2 \AA . We also propose that the (111) monatomic step exhibits similar dimerization, which should lead to a periodicity of 10.2 \AA on the InP(110) surface. At the present we are unable to determine whether the dimerized atoms in monatomic steps are In pairs or P pairs; theoretical work on this question is in progress.

In recent studies of the InAs(110) surface, we have searched for and found such periodicities on monatomic steps — which will be reported soon [4]. Presumably the same edge-reconstruction effect will be present in InP. We note also that not all steps observed are monatomic, and that models of these larger steps need to be developed [5].

It is worth remarking that the InP(110) surface is considerably more difficult to image with STM than either InAs(110) or InSb(110). This was unanticipated, and, while at first we thought it might have been related to the quality of our samples, we now suspect that it may be related to the ionicity of the material, since InSb was easy to image and InAs intermediate. We currently have no explanation of this.

IV. CONCLUSIONS

For cleaved InP(110) surfaces we observed the expected 1×1 surface reconstruction which is consistent with the standard model of this surface: the anions rotate up out of the surface, almost in a rigid rotation, by about 29° [6]. In addition we observed steps running in preferred directions on this surface: Step edges were found to run in the (110), (111), and (112) directions. Model calculations are under way to determine the energetics of formation of the various steps.

Periodicity along the (111) and (112) steps is a natural consequence of the Dimer Models we have proposed for the step-edges' relaxation. Model calculations are underway to determine if the dimers along the (111) and (112) steps are III-III or V-V dimers. The study of these steps appears to be a very interesting scientific problem with technological implications.

Acknowledgements — We are grateful to the U.S. Office of Naval Research and the U.S. Army Research Office for their support of this work (Contract Nos. N00014-92-J-1425 and DAAL03-91-G-0054).

REFERENCES

† Present address.

- [1] Ph. Ebert, G. Cox, U. Poppe, and K. Urban, *J. Ultramicroscopy*, **42-44**, 871 (1992).
- [2] Y. Liang, Ph.D. Thesis, University of Notre Dame, 1991. Available from University Microfilms, Ann Arbor, Michigan.
- [3] Y. Liang, W. E. Packard, and J. D. Dow, *J. Vac. Sci. Technol.* **B9**, 730 (1991).
- [4] Y. Liang, W. E. Packard, J. D. Dow, and G. J. Lapeyre, to be published.
- [5] See, for example, the polyatomic step in Fig. 2.
- [6] S. Y. Tong, A. R. Lubinsky, B. J. Mrstik, and M. A. Van Hove, *Phys. Rev. B* **17**, 3303 (1978); D. J. Chadi, *Phys. Rev. B* **18**, 1800 (1978); D. J. Chadi, *Phys. Rev.* **19**, 2074 (1979). See also the recent controversy over whether the surface relaxation angle depends on ionicity or not: Arguing for a dependence on ionicity are R. V. Kasowski, M.-H. Tsai, and J. D. Dow, *J. Vac. Sci. Technol.*, **B 5**, 953 (1987); M.-H. Tsai, J. D. Dow, R.-P. Wang, and R. V. Kasowski, *Phys. Rev. B* **40**, 9818 (1989); *Superlatt. Microstruct.* **6**, 431 (1989). J. L. A. Alves, J. Hebenstreit, and M. Scheffler, *Phys. Rev. B* **44**, 6188 (1991), supported by low-energy positron diffraction data of X. M. Chen, G. R. Brandes, K. F. Canter, C. B. Duke, D. Paton, W. K. Ford, and D. L. Lessor, *Bull. Amer. Phys. Soc.* **37**, 167 (1992). Arguing against such a dependence are C. B. Duke, R. J. Meyer, and P. Mark, *J. Vac. Sci. Technol.* **17**, 971 (1980); W. Chen, M. Dumas, S. Ahsan, A. Kahn, C. B. Duke, and A. Paton, *J. Vac. Sci. Technol. A* **10**, 2071 (1992); and A. Kahn, S. Ahsan, W. Chen, M. Dumas, C. B. Duke, and A. Paton, *Phys. Rev. Letters* **68**, 3200 (1992).

Random and ordered defects on ion-bombarded Si(100)-(2x1) surfaces.

H. Feil, H.J.W. Zandvliet
Philips Research Laboratories, P.O.Box 80.000
5600 JA Eindhoven, The Netherlands

M.-H. Tsai, John D. Dow and I.S.T. Tsong
Department of Physics and Astronomy, Arizona State University
Tempe, AZ 85287-1504

Abstract

Clean surfaces of Si(100)-(2x1) were bombarded by 3keV Ar⁺ ions at doses 10¹¹-10¹³ ions cm⁻². Scanning tunneling microscopy (STM) images of the bombarded surfaces showed random defects in the form of missing dimers or 'craters'. These defects ordered into line defects perpendicular to the dimer rows upon annealing the surface at temperatures between 600 °C and 850 °C for 2 minutes. Molecular Dynamics simulations were performed to explain the shapes and sizes of the observed craters and also to examine the stability of ordered defects. Our calculations showed a small energy difference between line defects along and perpendicular to the dimer rows, with a lower energy favouring the latter, in agreement with STM observations.

PACS numbers: 61.80.Jh; 68.55.Ln; 79.20.Rf

In a recent experiment in which we bombarded Si(100)-(2x1) surfaces with 3keV Ar⁺ ions at low doses, i.e. $\sim 10^{12}$ ions cm⁻² or $\sim 10^{-3}$ monolayer (ML), at room temperature, we reported the observation of random defects which ordered into line defects upon annealing the bombarded surfaces to 750 °C for 2 minutes¹. In another experiment by Bedrossian and Klitsner², Si(100)-(2x1) surfaces were bombarded by 225 eV Xe⁺ ions at high doses, i.e. 10^{15} ions cm⁻², at 450 °C. They observed retraction of the S_B edges, and subsequent appearance of vacancy islands on the A terraces upon further sputtering. Here we use Chadi's notation³ of S_A and S_B referring to step edges parallel and perpendicular to the dimer rows of the upper terrace respectively, and A and B terraces referring to those domains with dimer rows parallel and perpendicular to the step edges respectively. Our low dose experiment is illustrated in Fig.1. The starting Si(100)-(2x1) surface was remarkably free of any metal contamination which could give rise to line defects perpendicular to the dimer rows⁴. Fig.1(a) shows an image of such a surface taken by scanning tunneling microscopy (STM), with single missing dimers being the predominant defects. Fig.1(b) shows the surface after bombardment by 3keV Ar⁺ ions at normal incidence with a dose of 1.5×10^{12} ions cm⁻². A higher concentration of random defects was observed, some of which contain multiple missing dimers. When a bombarded surface was annealed at 600 °C for 2 minutes, the random defects appear to order into line defects perpendicular to the dimer rows, as shown in Fig.1(c). Annealing at higher temperatures, 750 °C and 850 °C for 2 minutes, has the same effect, as shown in Fig.1(d). When the bombarded surface was annealed

to 1200 °C for several seconds, the surface was completely restored to that shown in Fig.1(a), without any trace of line defects. We did not observe ordering of the random defects when we annealed the surface at 500 °C for 2 minutes. This implies that the threshold temperature for ordering lies between 500 °C and 600 °C, which is higher than the 450 °C observed by Bedrossian and Klitsner² for vacancy islands formation during high dose bombardment. This also implies that we have studied the formation and ordering of random defects separately. Interestingly, the vacancy islands, which have much larger areas than the line defects, have their long edges parallel to the dimer rows, in contrast to our line defects which are perpendicular to the dimer rows.

In this report, we compare our STM images with the results of molecular dynamics (MD) simulations in order to understand the mechanisms which lead to the formation of the random and ordered defects on the surface bombarded by low dose Ar⁺ ions.

In the classical MD simulations we have bombarded a dimerized Si(100) surface with individual 3 keV Ar⁺ ions. The microcrystallite consists of 12 layers of 32 atoms each. Periodic boundary conditions are applied in order to minimize boundary effects. The bottom layer atoms are coupled to their initial positions with a harmonic force. The value of the force constant is 10^{-8} Nm^{-1} . A temperature control is added to mimic the heat flow to the bulk. The method described by Berendsen et al⁵. is used to couple all the atoms of the crystallite to an external bath at constant temperature. In the simulation, the coupling is to a bath at $T = 300\text{K}$ with a time constant $\tau = 400\text{fs}$. With this value the crystallite is cooled

down to 300 K within a few ps after the ion impact. In order to correct for the dissipation of energy due to the shock wave shortly after the impact, the potential energy build up in the bottom atoms is removed from these atoms as long as their temperature exceeds the temperature of the external bath. In case of events causing large surface damage, a larger crystallite is used containing 128 Si atoms in each layer. This size is large enough to prevent interference due to the periodic boundary conditions and the finite size of the crystallite. The Si-Si interactions are described by the Stillinger and Weber many-body potential⁶. To incorporate a more repulsive Si-Si interaction at short internuclear separations, the potential is splined between $r = 1.09$ Å and $r = 1.59$ Å to a Moliere potential with a screening length of 0.83 times the Firsov value⁷. The attractive Ar-Ar and Si-Ar interactions are negligible under the experimental conditions. The non-bonding Ar-Si and Ar-Ar interactions are described by a Moliere potential, also with a screening length of 0.83 times the Firsov value.

A set of 30 trajectories is developed by random sampling of the representative area of the Si(100) surface. With every new trajectory, a fresh surface is bombarded with the ion. This approach simulates the low dose experiment. In the simulated 30 events we have observed 21 sputtered atoms and 57 Si atoms escaped through the bottom layer of the crystallite. The sputter yield compares well with the MD data of Smith et al.⁸ and is somewhat lower than the experimental high dose yield of ~ 1 atom/ion⁹. This implies that only about one-third of the surface vacancies are created by sputter removal. The remaining vacancies

are formed because Si atoms in the top layers are pushed into the bulk.

In six cases the simulation produced no surface damage. In the remaining simulations, we observed altogether 33 missing dimers, 25 defect dimers, 19 adatoms and 11 adclusters. The damage is in the form of 17 small craters, 8 medium size craters and 1 big crater. In a few cases the ion impact created more than one crater as shown in Fig.2(a). A small crater corresponds to the area of about one dimer. A medium crater corresponds to a damaged area of about 2 dimers while a large crater has an area of about 8 dimers. The classification is rather arbitrary and sometimes it is difficult to classify a crater in any one of the three categories. Examples of small, medium and large craters are given in Fig.2(b,c,d).

Our simulations produced 26 craters from 30 ion impacts, i.e. ~ 1 crater per impact. From our STM images in Fig.1, the clean surface in Fig.1(a) shows ~ 60 defects, represented by dark spots in the image; while the bombarded surface in Fig.1(b) shows ~ 125 defects or dark spots of various sizes. There is an increase of ~ 65 defects after bombardment. The ion dose in Fig.1(b) was 1.5×10^{12} ions cm^{-2} , which translates into ~ 10 ion impacts on an area of the size shown in Fig.1(b). So the number of additional defects is six times that of the ion impacts. From our STM images taken on Si(100)-(2x1) surfaces bombarded by doses varying from 7×10^{11} to 6×10^{12} ions cm^{-2} , we observed consistently more defects produced by the bombardment than the number of ion impacts. This sharply contrasts our observations on the Si(111)-(7x7) surface¹, on which we found the ratio of defects (or craters) to ion impacts was ~ 1 . The origin of this discrepancy could be that some of the

defects produced on the Si(100)-(2x1) surface may be electronic in origin rather than topographic, which cannot be shown in our classical MD simulations.

It is interesting to compare the large craters observed in the STM images with the large simulated crater shown in Fig.2(b). Fig.3 shows two large experimental craters on the same scale as that in Fig.2(b). There is a remarkable resemblance between experiment and simulation. In the simulated crater, we observe clusters of adatoms in the vicinity of the crater. We also observe large bright spots, which may be due to adclusters, near the large craters in the STM images.

Annealing at temperatures at or above 600 °C causes the random defects to order into narrow line defects as shown in Fig.1(c) and (d). The origin of these line defects may be explained if we assume a preferential vacancy mobility along the dimer rows¹⁰, similar to the mobility of Si adatoms^{11,12}, and the attractive interaction of the vacancies. The question of whether the line defects should be perpendicular or parallel to the dimer rows is examined by performing a microscopic study using a quantum-mechanical MD method. The advantage of using this method over the conventional total energy calculational method is that atomic positions are automatically optimized according to Newton's laws of motion. In contrast, the conventional total energy methods need to preconceive some preferred geometries. The MD method employed in this study is the *ab initio* real-space method of Sankey and Niklewski¹³, which has been shown to work well for various systems of carbon and silicon^{14,15,16}.

In this study, the Si(100) surface is modeled by a five-layer-slab repeated slab (super cell) model; the atoms in the bottom layer are assigned with huge masses and attached with hydrogen-like atoms to saturate their dangling bonds so that they are motionless and are regarded as bulk atoms. The observed bulk lattice constant of Si, 5.43072 \AA ¹⁷, is used to set up the two-dimensional lattice. Chadi¹⁸ has shown that for the Si(100) surface atomic relaxations extend over the first five layers. Since the atomic displacement for the fifth-layer atom was calculated to be only 0.034 \AA ¹⁸, we believe the use of a fixed fifth layer may be adequate for studying relative preference between perpendicular and parallel line defects. (Here, "perpendicular" and "parallel" are defined with respect to the dimer rows). The line defect is modeled by a *periodic array* of infinitely long missing atomic lines. Fig. 4(a) and (b) correspond to line defects which are perpendicular and parallel to dimer rows respectively. In the former case, denoted as case (i), the missing atomic lines are separated by three surface atoms (or three pairs of dimers). The unit cell contains thirty eight atoms, i.e. six in the surface layer and eight per layer in the second to fifth layers. As shown in Fig.4(a), exposed second layer atoms have freedom to form dimers; whether they form dimers is to be determined by the MD simulations, which let all atoms except those in the bottom layer settle to their most stable positions. As for the case shown in Fig.4(b), denoted as case (ii), the twin missing atomic lines (or missing dimer rows) are separated by three dimer rows. The choice of twin missing atomic lines is to keep the ratio between the number of missing atoms and surface atoms in a unit cell the same as that for case (i) so that the comparison

of total energies is meaningful. We choose a unit cell twice as large as that of case (i). There are seventy-six atoms per unit cell; twelve in the surface layer and sixteen per layer in the second to fifth layers. This choice of a doubled unit cell is to allow the exposed second-layer atoms freedom to form dimers. For both cases (i) and (ii) we use the single two-dimensional special point of Cunningham¹⁹ for a rectangular lattice and its reflectionally symmetric points with respect to x and y axes and the inversion symmetric point to optimize atomic positions. To compare total energies (per atom) between cases (i) and (ii), we find that the use of sixteen two-dimensional special points of Cunningham¹⁹ is quite adequate. We have also tested the use of sixty-four special points and it essentially yields the same results.

Fig.4(a) and (b) show the lateral displacements of surface- and second-layer atoms from their ideal unrelaxed atomic positions. In both cases (i) and (ii) dimerization directions of surface atoms and exposed second-layer atoms can be seen perpendicular to each other as stated previously. Surface atoms form buckled (not shown in Fig.4) asymmetric dimers similar to those discussed by Chadi¹⁸. In case (i), the second layer dimerization is not very pronounced and the atomic pairs have bond lengths (2.86Å) much larger than that of surface dimers (2.36Å). This is because each exposed second-layer atom is still bonded to and drawn towards a surface atom at either edge of the line defect. We have performed charge density calculations and find that the charge density is significantly large in the central region of each atom-pair in the exposed layer to indicate that the atom-pairs indeed form

dimers through their single dangling bonds. It is interesting to note that in case (ii), the two second-layer dimer lines in the defect are not in phase. They are approximately out of phase by about 180° . This arrangement exerts less strain on third-layer atoms bridged between these two second-layer dimer lines than when they are in phase.

We find that the total energy for case (i) is about 0.011 eV/atom lower than that for case (ii) favoring line defects perpendicular to dimer rows as shown in the STM images Fig.1(c) and (d). The lower total energy for case (i) may be qualitatively understood from the shorter bonding distance (and hence stronger bonding) between an exposed second-layer atom and a surface atom at either edge of the line defect as shown in Fig.4(a). However, the preference for the case (i) is partly compensated by the restriction of exposed-second-layer dimerization, as stated earlier, and by the interruption of the (2x1) dimer rows. In contrast, the exposed second-layer atoms in case (ii) have less constraint to form dimers and have no interruption of dimer rows as shown in Fig.4(b). This may be the reason why the calculated total energy difference is small.

The observations by Bedrossian and Klitsner² appear to contradict the above results of our calculations, since they found monolayer deep vacancy islands elongated parallel to the dimer rows. However, it must be remembered that their experiment was conducted at 450°C with Xe^+ ions bombarding the surface at a dose several orders of magnitude higher than in our experiment. In their case, due to the high dose bombardment, the mobility of the vacancies is enhanced similar to the enhanced mobility of surface atoms in ion-beam

assisted deposition²⁰. Moreover, the mean vacancy-migration barrier is lower due to the high density of vacancies with fewer neighbouring dimers. Both effects lead to the establishment of an equilibrium situation without invoking any presumption of anisotropic vacancy diffusion. The elongation of their vacancy islands along the dimer rows is expected since the energy of the S_A step is lower than that of the S_B step^{21,22}.

In summary, we have obtained good agreement between molecular-dynamics simulations and STM images of random and ordered defects produced by energetic ion impacts on the Si(100)-(2x1) surface.

I.S.T. Tsong thanks Philips Research Laboratories for the award of a van Houten Fellowship. M.-H Tsai and J.D. Dow acknowledge support from U.S. Army Research Office (DAAL03-91-G-0054).

Figure Captions

Fig. 1 Filled-state STM images of Si(100)-(2x1) surfaces taken at sample bias -2V and tunnel current 0.5 nA. (a) Clean surface prior to bombardment. Scan area = 28nm x 28nm. (b) After bombardment by 3keV Ar⁺ ions at a dose of 1.5×10^{12} ions cm⁻². Scan area = 26nm x 26nm. (c) Bombarded surface after annealing for 2 minutes. Scan area = 22nm x 22nm. (d) Bombarded surface after annealing at 750°C for 2 minutes. Scan area = 40nm x 40nm.

Fig. 2 Ion impact craters produced by molecular dynamics simulations. (a) A double crater. (b) A large crater. (c) A medium crater. (d) A small crater. The craters in (b) and (c) appear double because of periodic boundary conditions.

Fig. 3 STM images of two large craters caused by a 3keV Ar⁺ ion bombardment. Area = 6nm x 6nm.

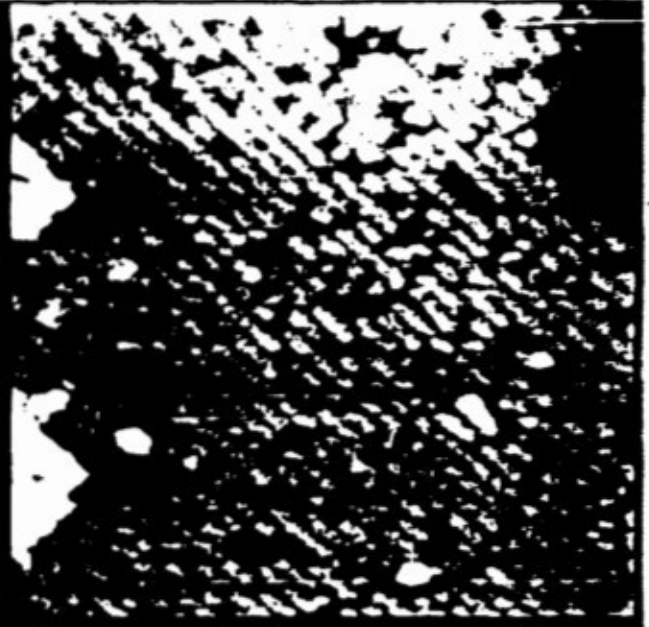
Fig. 4 Molecular-dynamics simulations of a periodic array of line defects on the Si(100)-(2x1) surface. (a) Line defect perpendicular to dimer rows, and (b) line defect parallel to dimer rows. The small crosses and the solid dots are ideal unrelaxed positions for surface and second-layer atoms respectively. The rectangle enclosed by dashed lines is the unit cell.

(1991)

- 17 CRC Handbook of Chemistry and Physics, Ed. by D.R. Lide, 72nd edition (Boca raton, Ann Arbor, Boston, 1991-1992)
- 18 D.J. Chadi, Phys.Rev.Lett. 43, 43 (1979)
- 19 S.L.Cunningham, Phys.Rev.B10, 4988 (1974)
- 20 Ion Beam Assisted Film Growth, edited by T. Itoh (Elsevier, New York, 1989)
- 21 B.S. Swartzentruber, Y-M. Mo, R. Kariotis, M.G. Lagally and M.B. Webb, Phys.Rev.-Lett. 65, 1913 (1990)
- 22 H.J.W. Zandvliet, H.B. Elswijk, E.J. van Loenen and D. Dijkkamp, Phys.Rev.B (to be published)

Fig 1

a



c

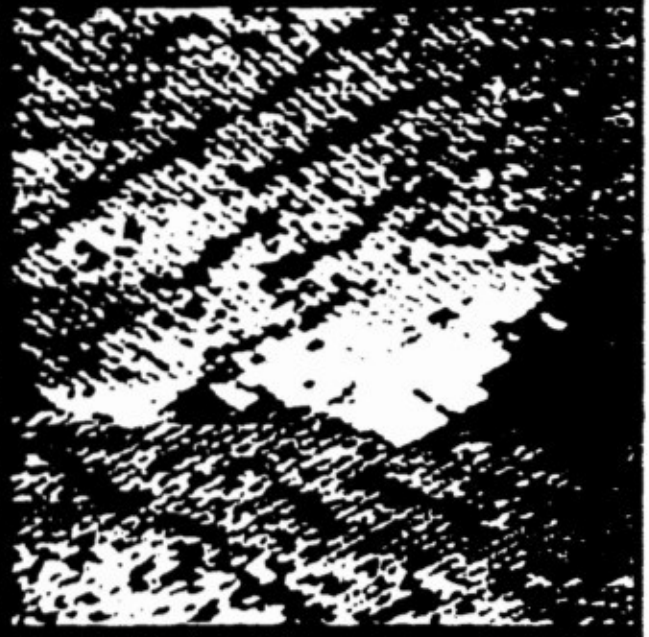
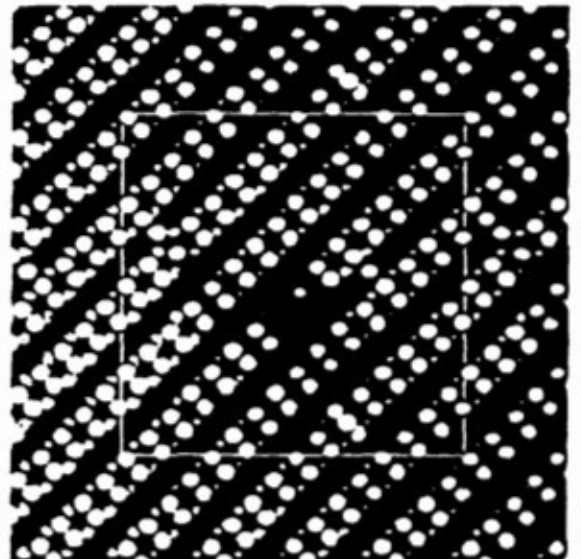
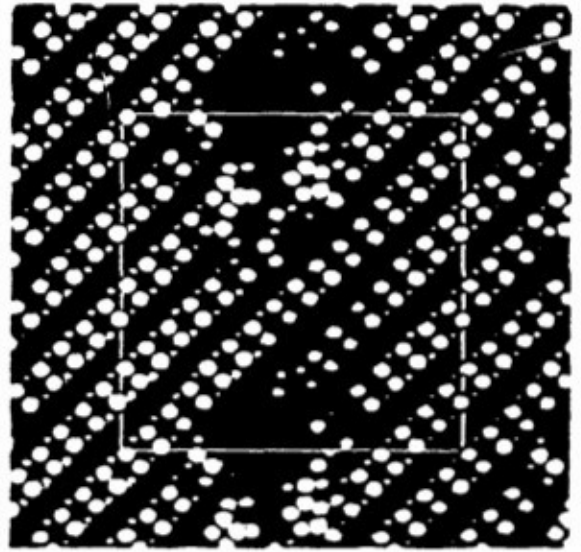
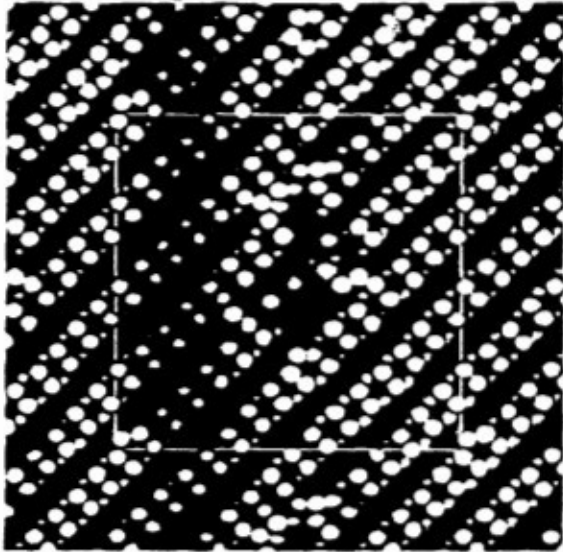


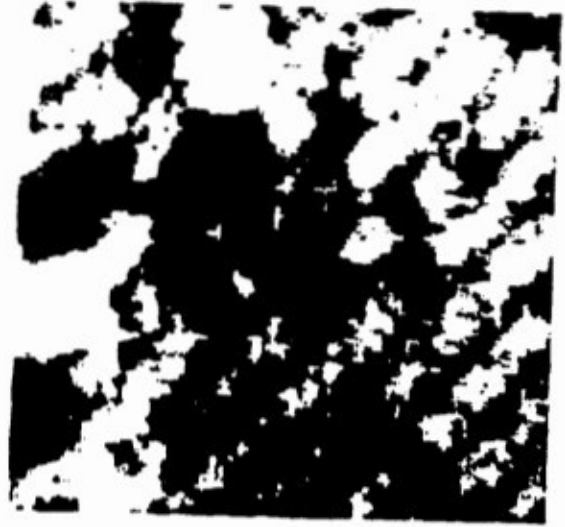
Fig 2



b

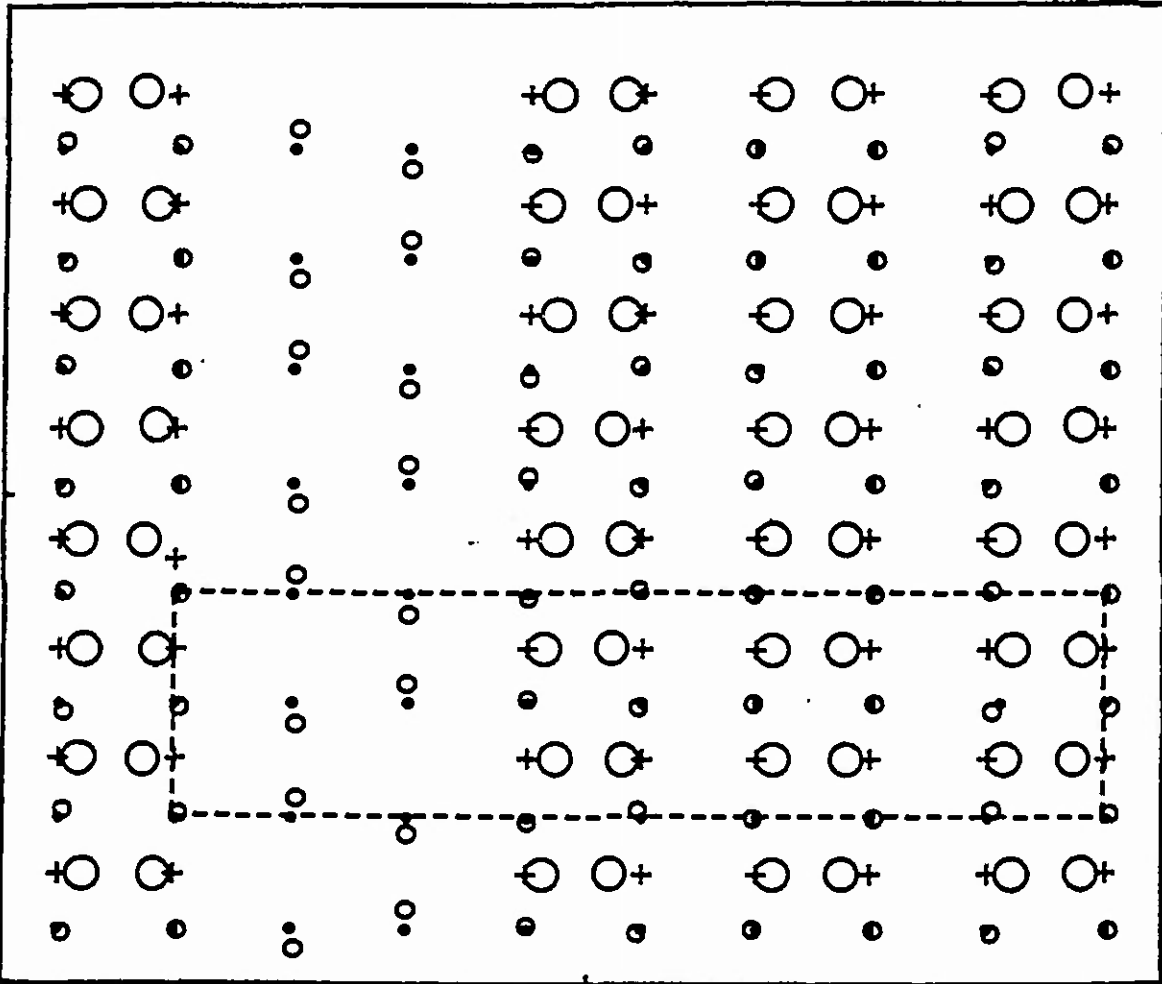
d

Fig. 3

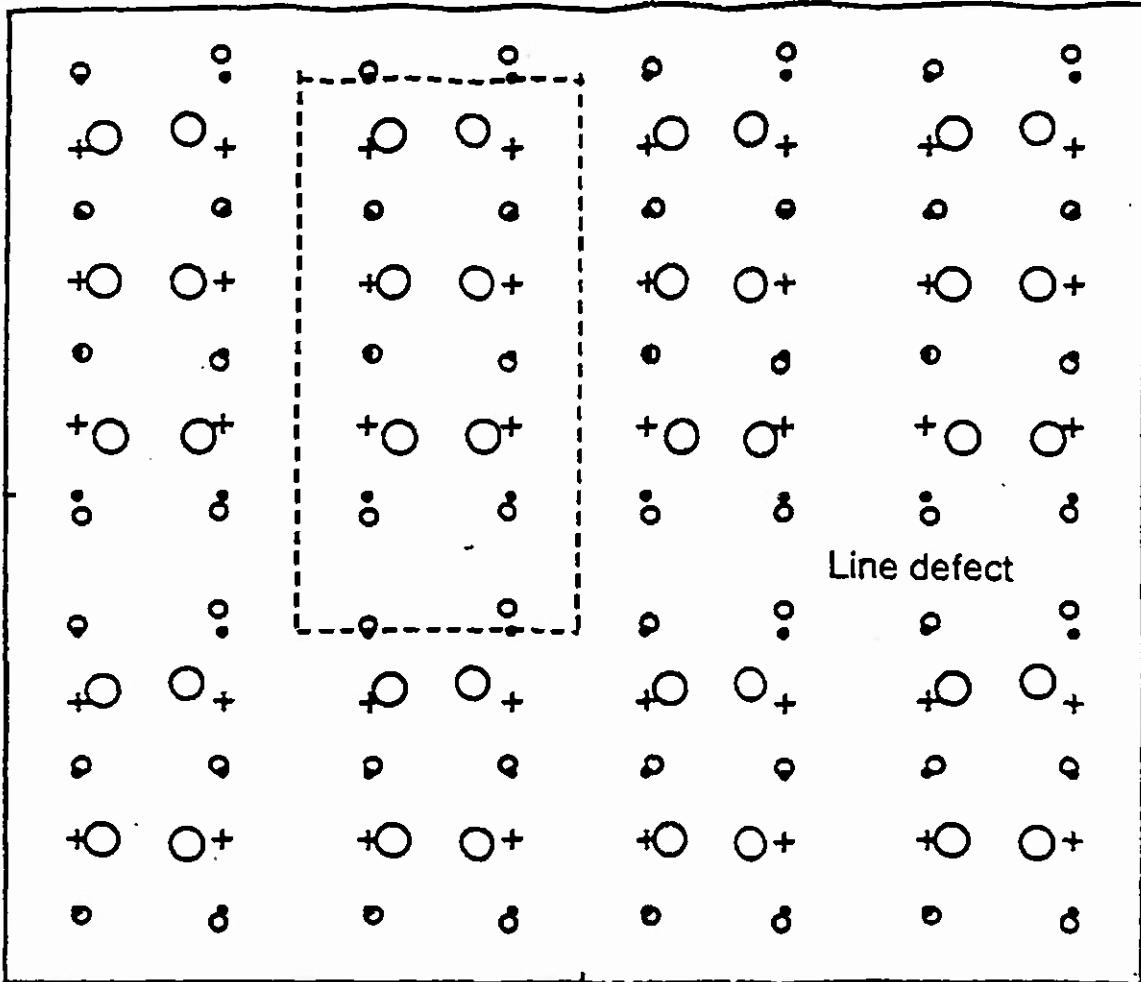


(b)

Line defect



(a)



Random and Ordered Defects on Ion-Bombarded Si(100)-(2×1) Surfaces

H. Feil and H. J. W. Zandvliet

Philips Research Laboratories, P.O. Box 80.000, 5600 JA Eindhoven, The Netherlands

M.-H. Tsai, John D. Dow, and I. S. T. Tsong

Department of Physics and Astronomy, Arizona State University, Tempe, Arizona 85287-1504

(Received 29 April 1992)

Scanning tunneling microscopy (STM) images of Si(100)-(2×1) surfaces bombarded by low-dose 3-keV Ar⁺ ions showed random defects which ordered into line defects perpendicular to the dimer rows upon annealing at elevated temperatures. Molecular-dynamics simulations were performed to explain the shapes and sizes of the observed random defects and also to examine the stability of ordered defects. Our simulations showed good agreement with STM observations.

PACS numbers: 61.80.Jh, 68.55.Ln, 79.20.Rf

The process of sputtering, which involves the removal of individual atoms and molecules from a surface by energetic ions, has been a subject of interest for many decades. With the advent of scanning tunneling microscopy (STM), one has the means of viewing the surface damage due to sputtering with atomic resolution. In a recent experiment in which we bombarded Si(100)-(2×1) surfaces with 3-keV Ar⁺ ions at low doses, i.e., $\sim 10^{12}$ ions cm⁻² or $\sim 10^{-3}$ monolayer (ML), at room temperature, we reported the observation of random defects which ordered into line defects upon annealing the bombarded surfaces to 750 °C for 2 min [1]. The low-dose experiment is illustrated in Fig. 1. The starting Si(100)-(2×1) surface was remarkably free of any metal contamination which could

give rise to line defects perpendicular to the dimer rows [2]. Figure 1(a) shows an STM image of such a surface, with single missing dimers being the predominant defects. Figure 1(b) shows the surface after bombardment by 3-keV Ar⁺ ions at normal incidence with a dose of 1.5×10^{12} ions cm⁻², equivalent to ~ 0.002 ML coverage. A higher concentration of random defects was observed, some of which contain multiple missing dimers. When a bombarded surface was annealed at 600 °C for 2 min, the random defects appeared to order into line defects perpendicular to the dimer rows, as shown in Fig. 1(c). Annealing at higher temperatures, 750 and 850 °C for 2 min, produced the same effect as shown in Fig. 1(d). When the bombarded surface was annealed at 950 °C for 2 min, or flashed to 1200 °C for a few seconds, the surface was completely restored to that shown in Fig. 1(a), without any trace of line defects, thus ruling out the possibility of metal contamination which invariably worsens with each annealing cycle. We did not observe any ordering of the random defects when we annealed the surface at 500 °C for 2 min. This implies that the threshold temperature for ordering lies between 500 and 600 °C. Over 100 STM images were taken in our experiment and consistent results were obtained.

The possibility exists that the line defects are not due to ordering of surface vacancies, but arise from the ordering of implanted Ar atoms diffusing to the surface during annealing. However, previous ellipsometry studies of desorption of implanted Ar from Si surfaces [3] show that desorption takes place at temperatures as low as 400 °C, reaching a maximum at 600 °C. Complete desorption is achieved at 800 °C and the Si surface returns to its original state [4]. These results do not agree with our observation that ordering occurs between 600 and 850 °C, and the line defects only disappear at 950 °C or upon flashing the surface to 1200 °C. Analysis of fourteen STM images taken before and after annealing shows that the number of vacancies increases on average by $\sim 15\%$ after annealing. A plausible cause for the increase is the migration of buried vacancies to the surface during the annealing process, or it could be the result of random sampling of the surface because the STM did not

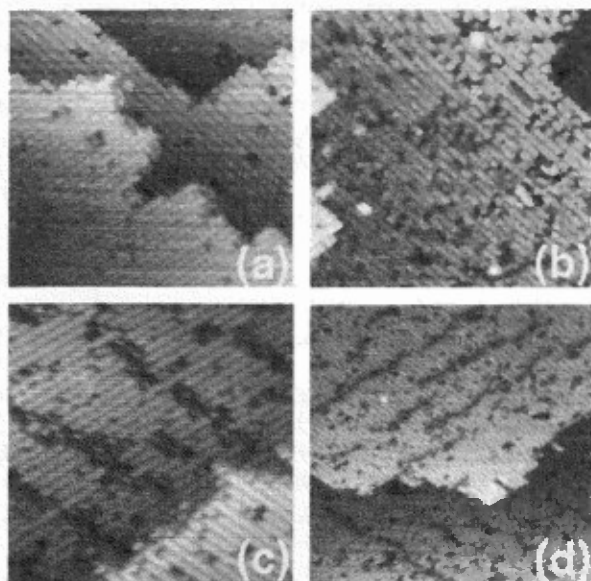


FIG. 1. Filled-state STM images of Si(100)-(2×1) surfaces taken at sample bias of -2 V and tunnel current 0.5 nA. (a) Clean surface prior to bombardment. Scan area is 28 nm×28 nm. (b) After bombardment by 3-keV Ar⁺ ions at a dose of 1.5×10^{12} ions cm⁻². Scan area is 26 nm×26 nm. (c) Bombarded surface after annealing at 600 °C for 2 min. Scan area is 22 nm×22 nm. (d) Bombarded surface after annealing at 750 °C for 2 min. Scan area is 40 nm×40 nm.

image the same localized area after annealing. The Gaussian distribution of the Ar^+ ions in the beam spot impacting the surface could also give rise to the counting discrepancy.

In this Letter, we compare our STM images with the results of molecular-dynamics (MD) simulations in order to understand the mechanisms which lead to the formation of the random and ordered defects on the surface bombarded by a low dose of Ar^+ ions.

In the classical MD simulations we have bombarded a dimerized $\text{Si}(100)$ surface with individual 3-keV Ar^+ ions. The microcrystallite consists of 12 layers of 32 atoms each. Periodic boundary conditions are applied in order to minimize boundary effects. The bottom-layer atoms are coupled to their initial positions with a harmonic force. The value of the force constant is 10^{-8} Nm^{-1} . A temperature control is added to mimic the heat flow to the bulk. The method described by Berendsen *et al.* [5] is used to couple all the atoms of the crystallite to an external bath at constant temperature. In the simulation, the coupling is to a bath at $T=300 \text{ K}$ with a time constant $\tau=400 \text{ fs}$. With this value the crystallite is cooled down to 30 K within a few ps after the ion impact. In order to correct for the dissipation of energy due to the shock wave shortly after the impact, the potential energy buildup in the bottom atoms is removed from these atoms as long as their temperature exceeds the temperature of the external bath. In the case of events causing large surface damage, a larger crystallite is used containing 128 Si atoms in each layer. This size is large enough to prevent interference due to the periodic boundary conditions and the finite size of the crystallite. The Si-Si interactions are described by the Stillinger and Weber many-body potential [6]. To incorporate a more repulsive Si-Si interaction at short internuclear separations, the potential is splined between $r=1.09$ and 1.59 \AA with a Moliere potential with a screening length of 0.83 times the Firsov value [7]. The attractive Ar-Ar and Si-Ar interactions are negligible under the experimental conditions. The nonbonding Ar-Si and Ar-Ar interactions are described by a Moliere potential, also with a screening length of 0.83 times the Firsov value. The individual trajectories are sensitive to the details of the short-range interactions such as small variations of the impact points of the incoming ion. Consequently, we performed statistical analysis on the simulations in much the same manner as we did on the experimental results.

A set of 30 trajectories is developed by random sampling of the representative area of the $\text{Si}(100)$ surface. With every new trajectory, a fresh surface is bombarded with the ion. This approach simulates the low-dose experiment. In the simulated 30 events we have observed 21 sputtered atoms. The sputter yield compares well with the MD data of Smith, Harrison, and Garrison [8] and is somewhat lower than the experimental high-dose yield of ~ 1 atom/ion [9]. Only about one-third of the surface vacancies are created by sputter removal. The remaining

vacancies are formed because Si atoms in the top layers are recoiled into the bulk. These recoil Si atoms are the beginning of collision cascades and in the 30 events, 57 Si atoms escaped through the bottom layer of the crystallite.

In six cases the simulation produced no surface damage. In the remaining simulations, we observed altogether 33 missing dimers, 25 defect dimers, 19 adatoms, and 11 adclusters. The damage is in the form of 17 small craters, 8 medium size craters, and 1 large crater. In a few cases, the ion impact created more than 1 crater, as shown in Fig. 2(a). A small crater corresponds to the area of about 1 dimer. A medium crater corresponds to a damaged area of about 2 dimers, while a large crater has an area of about 8 dimers. The classification is rather arbitrary and sometimes it is difficult to classify a crater in any one of the three categories. Examples of small, medium, and large craters are given in Figs. 2(b)–2(d).

Our simulations produced 26 craters from 30 ion impacts, i.e., ~ 1 crater per impact. From our STM images in Fig. 1, the clean surface in Fig. 1(a) shows ~ 60 defects, represented by dark spots in the image, while the bombarded surface in Fig. 1(b) shows ~ 125 defects or dark spots of various sizes. There is an increase of ~ 65 defects after bombardment. The ion dose in Fig. 1(b) was $1.5 \times 10^{12} \text{ ionscm}^{-2}$, which translates into ~ 10 ion impacts on an area of the size shown in Fig. 1(b). So the number of additional defects is 6 times that of the ion impacts. From our STM images taken on $\text{Si}(100)$ – (2×1) surfaces bombarded by doses varying from 7×10^{11} to $6 \times 10^{12} \text{ ionscm}^{-2}$, we observed consistently more defects produced by the bombardment than the number of ion impacts. This sharply contrasts our observations on the $\text{Si}(111)$ – (7×7) surface [1], on which we found the ratio

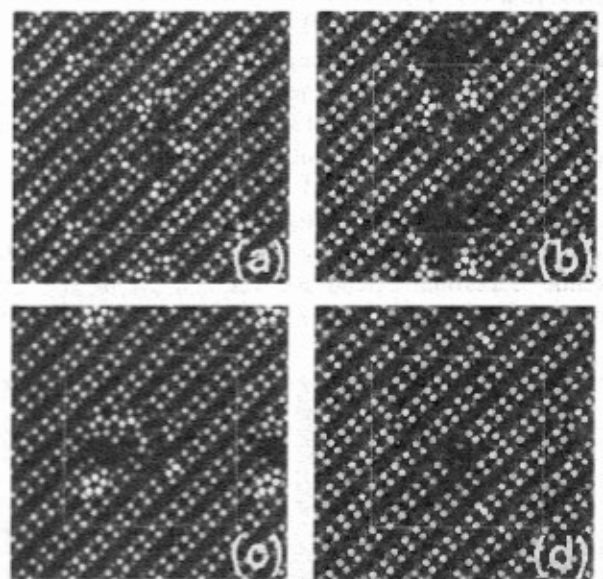


FIG. 2. Ion-impact craters produced by molecular-dynamics simulations. (a) A double crater. (b) A large crater. (c) A medium crater. (d) A small crater. The craters in (b) and (c) appear double because of periodic boundary conditions.

of defects (or craters) to ion impacts was ~ 1 . The origin of this discrepancy could be that on Si(100), each ion impact creates more than 1 site from which sputtering occurs, as MD simulations show in Fig. 2(a). Some of the defects generated may also be electronic in origin rather than topographic, and they are unrelated to sputtering.

It is interesting to compare the large craters observed in the STM images with the large simulated crater shown in Fig. 2(h). Figure 3 shows two large experimental craters on the same scale as that in Fig. 2(b). There is a remarkable resemblance between experiment and simulation. In the simulated crater, we observe clusters of adatoms in the vicinity of the crater. We also observe large bright spots, which may be due to adclusters, near the large craters in the STM images.

Annealing at temperatures at or above 600°C causes the random defects to order into narrow line defects as shown in Figs. 1(c) and 1(d). A possible origin of these line defects could be a preferential mobility of vacancies on the surface along the dimer rows [10] as a consequence of the annealing temperature, and the attractive interaction of the vacancies. The question of whether the line defects should be perpendicular or parallel to the dimer rows is examined by performing a microscopic study using a quantum-mechanical MD method. The advantage of using this method over the conventional total-energy calculational method is that atomic positions are automatically optimized according to Newton's laws of motion. In contrast, the conventional total-energy methods need to preconceive some preferred geometries. The MD method employed in this study is the *ab initio* real-space method of Sankey and Niklewski [11], which has been shown to work well for various systems of carbon and silicon [12-14].

In this study, the Si(100) surface is modeled by a five-layer-slab repeated slab (supercell) model; the atoms in the bottom layer are assigned with huge masses and attached with hydrogenlike atoms to saturate their dangling bonds so that they are motionless and are regarded as bulk atoms. The observed bulk lattice constant of Si, 5.43072 \AA [15], is used to set up the two-dimensional lattice. Chadi [16] has shown that for the Si(100) surface atomic relaxations extend over the first five layers. Since the atomic displacement for the fifth-layer atom was cal-

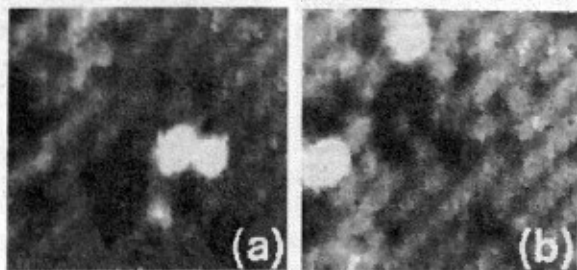


FIG. 3. STM images of two large craters caused by a 3-keV Ar^+ -ion bombardment. Area is $6 \text{ nm} \times 6 \text{ nm}$.

culated to be only 0.034 \AA [16], we believe the use of a fixed fifth layer may be adequate for studying relative preference between perpendicular and parallel line defects. (Here, "perpendicular" and "parallel" are defined with respect to the dimer rows.) The line defect is modeled by a *periodic array* of infinitely long missing atomic lines. Figures 4(a) and 4(b) correspond to line defects which are perpendicular and parallel to the dimer rows, respectively. Because of the usual computer constraints, we could realistically only consider the lower limit of the line-defect width. In the perpendicular case (i), the line defect is a single missing atomic line repeating itself periodically every fourth line. The unit cell contains 38 atoms, i.e., 6 in the surface layer and 8 per layer in the second to fifth layers. As shown in Fig. 4(a), exposed second-layer atoms have the freedom to form dimers; whether they form dimers is to be determined by the MD simulations, which allow all atoms except those in the bottom layer to settle to their most stable positions.

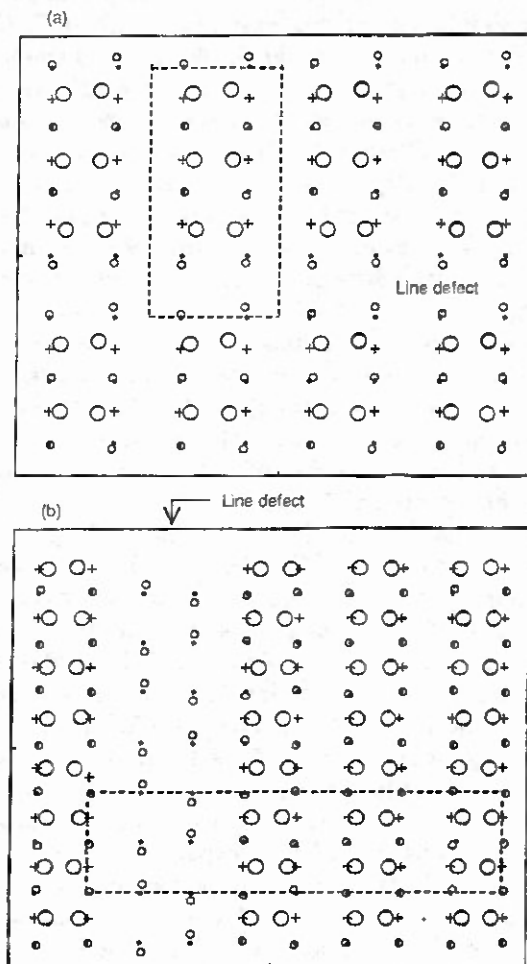


FIG. 4. Molecular-dynamics simulations of a periodic array of line defects on the Si(100)-(2 \times 1) surface. (a) Line defects perpendicular to dimer rows, case (i); and (b) line defect parallel to dimer rows, case (ii). The small crosses and the solid dots are ideal unrelaxed positions for surface- and second-layer atoms, respectively. The rectangle enclosed by dashed lines is the unit cell.

For the parallel case shown in Fig. 4(b), denoted as case (ii), the periodic line defects are in the form of a single missing dimer row (i.e., twin missing atomic lines) repeating every fourth dimer row. The choice of twin missing atomic lines is to keep the ratio between the number of missing atoms and surface atoms in a unit cell the same as that for case (i) so that the comparison of total energies is meaningful. We choose a unit cell twice as large as that of case (i). There are 76 atoms per unit cell, 12 in the surface layer and 16 per layer in the second to fifth layers. This choice of a doubled unit cell is to allow the exposed second-layer atoms freedom to form dimers. For both cases (i) and (ii) we use the single two-dimensional special point of Cunningham [17] for a rectangular lattice and its reflectionally symmetric points with respect to x and y axes and the inversion symmetric point to optimize atomic positions. To compare total energies (per atom) between cases (i) and (ii), we find that the use of 16 two-dimensional special points of Cunningham [17] is quite adequate. We have also tested the use of 64 special points and it essentially yields the same results.

Figures 4(a) and 4(b) show the lateral displacements of surface- and second-layer atoms from their ideal unrelaxed atomic positions. In both cases (i) and (ii) dimerization directions of surface atoms and exposed second-layer atoms can be seen perpendicular to each other as stated previously. Surface atoms form buckled (not shown in Fig. 4) asymmetric dimers similar to those discussed by Chadi [16]. In case (i), the second-layer dimerization is not very pronounced and the atomic pairs have bond lengths (2.86 Å) much larger than that of surface dimers (2.36 Å). This is because each exposed second-layer atom is still bonded to and drawn towards a surface atom at either edge of the line defect. We have performed charge-density calculations and find that the charge density is significantly large in the central region of each atom pair in the exposed layer to indicate that the atom pairs indeed form dimers through their single dangling bonds. It is interesting to note that in case (ii), the two second-layer dimer lines in the defect are not in phase. They are approximately out of phase by about 180°. This arrangement exerts less strain on third-layer atoms bridged between these two second-layer dimer lines than when they are in phase.

We find that the total energy for case (i) is about 0.011 eV/atom lower than that for case (ii), favoring line defects perpendicular to dimer rows as shown in the STM images Figs. 1(c) and 1(d). The lower total energy for case (i) may be qualitatively understood from the shorter bonding distance (and hence stronger bonding) between an exposed second-layer atom and a surface atom at either edge of the line defect as shown in Fig. 4(a). However, the preference for case (i) is partly compensated by the restriction of exposed-second-layer dimerization, as stated earlier, and by the interruption of the (2×1) dimer rows. In contrast, the exposed second-layer atoms in case

(ii) have less constraint to form dimers and have no interruption of dimer rows as shown in Fig. 4(b). This may be the reason that the calculated total energy difference is small.

In a recent report by Bedrossian and Klitsner [18], Si(100)-(2×1) surfaces were bombarded by 225-eV Xe⁺ ions at grazing incidence along the [110] direction at temperatures 400–450°C. They observed retraction of S_B step edges as well as monolayer-deep depressions or "vacancy islands" elongated parallel to the dimer rows. However, in contrast to the present report, the structures they observed are not equilibrium structures, but are structures stabilized at moderately high temperatures, i.e., ~450°C, by kinetic considerations, analogous with growth.

In summary, we have obtained good agreement between molecular-dynamics simulations and STM images of random and ordered defects produced by energetic ion impacts on the Si(100)-(2×1) surface.

We thank Peter Bedrossian for his useful comments and suggestions on the manuscript. I.S.T.T. thanks Philips Research Laboratories for the award of a van Houten Fellowship. M.-H.T. and J.D.D. acknowledge support from U.S. Army Research Office (DAAL03-91-G-0054).

- [1] H. J. W. Zandvliet, H. B. Elswijk, E. J. van Loenen, and I. S. T. Tsong, *Phys. Rev. B* **46**, 7581 (1992).
- [2] H. Niehus, U. K. Koehler, M. Copel, and J. E. Demuth, *J. Microsc.* **152**, 735 (1988).
- [3] A. H. M. Holtslag and A. van Silfhout, *Surf. Sci.* **187**, 36 (1987).
- [4] A. H. M. Holtslag, U. C. Slager, and A. van Silfhout, *Surf. Sci.* **152/153**, 1079 (1985).
- [5] H. J. C. Berendsen, J. P. M. Postma, W. F. van Gunsteren, A. DiNola, and J. R. Haak, *J. Chem. Phys.* **81**, 3684 (1984).
- [6] F. H. Stillinger and T. A. Weber, *Phys. Rev. B* **31**, 5262 (1985).
- [7] I. M. Torrens, *Interatomic Potentials* (Academic, New York, 1972).
- [8] R. Smith, D. E. Harrison, and B. J. Garrison, *Phys. Rev. B* **40**, 3979 (1989).
- [9] P. C. Zalm, *J. Appl. Phys.* **54**, 2660 (1983).
- [10] H. Kahata and K. Yagi, *Jpn. J. Appl. Phys.* **28**, L1042 (1989).
- [11] O. F. Sankey and D. J. Niklewski, *Phys. Rev. B* **40**, 3979 (1989).
- [12] O. F. Sankey, D. J. Niklewski, D. A. Drabold, and J. D. Dow, *Phys. Rev. B* **41**, 12750 (1990).
- [13] G. B. Adams and O. F. Sankey, *Phys. Rev. Lett.* **67**, 867 (1991).
- [14] G. B. Adams, J. B. Page, O. F. Sankey, K. Sinha, and J. Menendez, *Phys. Rev. B* **44**, 4052 (1991).
- [15] *CRC Handbook of Chemistry and Physics*, edited by D. R. Lide (CRC Press, Boca Raton, 1991–1992), 72nd ed.
- [16] D. J. Chadi, *Phys. Rev. Lett.* **43**, 43 (1979).
- [17] S. L. Cunningham, *Phys. Rev. B* **10**, 4988 (1974).
- [18] P. Bedrossian and T. Klitsner, *Phys. Rev. Lett.* **68**, 646 (1992).